Pattern formation in a four-ring reaction-diffusion network with heterogeneity

Ian Hunter [1,*] Michael M. Norton [2,*] Bolun Chen [3,4] Chris Simonetti,[1] Maria Eleni Moustaka [1]
Jonathan Touboul [3,5] and Seth Fraden [1,†]

[1]*Brandeis University Physics, Waltham, Massachusetts 02453, USA*
[2]*Center for Neural Engineering, Department of Engineering Science and Mechanics, The Pennsylvania State University,
University Park, Pennsylvania 16802, USA*
[3]*Volen National Center for Complex Systems, Brandeis University, Waltham, Massachusetts 02453, USA*
[4]*Department of Physics, Boston University, Boston Massachusetts 02215, USA*
[5]*Brandeis University Mathematics Department, Waltham, Massachusetts 02453, USA*

In networks of nonlinear oscillators, symmetries place hard constraints on the system that can be exploited to predict universal dynamical features and steady states, providing a rare generic organizing principle for far-from-equilibrium systems. However, the robustness of this class of theories to symmetry-disrupting imperfections is untested in free-running (i.e., non-computer-controlled) systems. Here, we develop a model experimental reaction-diffusion network of chemical oscillators to test applications of the theory of dynamical systems with symmeries in the context of self-organizing systems relevant to biology and soft robotics. The network is a ring of four microreactors containing the oscillatory Belousov-Zhabotinsky reaction coupled to nearest neighbors via diffusion. Assuming homogeneity across the oscillators, theory predicts four categories of stable spatiotemporal phase-locked periodic states and four categories of invariant manifolds that guide and structure transitions between phase-locked states. In our experiments, we observed that three of the four phase-locked states were displaced from their idealized positions and, in the ensemble of measurements, appeared as clusters of different shapes and sizes, and that one of the predicted states was absent. We also observed the predicted symmetry-derived synchronous clustered transients that occur when the dynamical trajectories coincide with invariant manifolds. Quantitative agreement between experiment and numerical simulations is found by accounting for the small amount of experimentally determined heterogeneity in intrinsic frequency. We further elucidate how different patterns of heterogeneity impact each attractor differently through a bifurcation analysis. We show that examining bifurcations along invariant manifolds provides a general framework for developing intuition about how chemical-specific dynamics interact with topology in the presence of heterogeneity that can be applied to other oscillators in other topologies.

I. INTRODUCTION

Network science unifies the study of disparate physical systems that can be cast as discrete sets of interacting dynamical units [1]. Here, we focus on networks of self-driven chemical oscillators, which use chemical fuel to exhibit far-from-equilibrium dynamics. This simple framework provides profound insights into systems ranging from electrical power grids to biological neural networks known as central pattern generators responsible for coordinating autonomous animal locomotion [2–7].

The design of networks that generate desired spatiotemporal patterns is a great challenge because universal organizing principles for far-from-equilibrium systems are exceedingly rare. Exploiting network symmetry is one way to meet this challenge. Symmetries place hard constraints on the network dynamics of self-driven oscillators by dictating that certain transient features and steady-state patterns *must* exist.

A class of results uses group theory to predict spatiotemporal patterns required by the spatial symmetry of the network [8–10]. One such result, the H/K theorem, enumerates all symmetry-derived patterns by including the temporal periodicity of the oscillators [3,11–15]. Significantly, these patterns are universal. They depend only on the coupling topology and are independent of all system-specific details regarding the nature of the nonlinear oscillators themselves and even whether or not the coupling is nonlinear. This class of theories has important implications for biology, leading to the ansatz that central pattern generators exploit symmetry [3], or in other words that "form follows function." However, these striking results derive from the strong assumption that nodes in the network and their interconnections are strictly identical [11,15]. Since the framework is powerful, knowing how to apply it to specific systems that are not strictly homogeneous is beneficial for understanding naturally occurring biological and chemical systems, developing control strategies [16], and designing new materials.

In this work we experimentally and theoretically explore the effect of frequency heterogeneity on the symmetry-required dynamics of a ring of four chemical oscillators.

---

*These authors contributed equally to this work.
†Corresponding author: fraden@brandeis.edu

Experimental studies exploring heterogeneity in networks of any kind are rare, but are necessary to assess the relevancy of symmetry-based theories to real-world networks. Here, we present a study of heterogeneity in a chemical reaction-diffusion network. These chemical networks play an important role in elucidating significant biological phenomena, such as morphogenesis [17] and central pattern generators in neural networks [2].

The influence of heterogeneity on synchronization dynamics is integral to the study of oscillator networks. Kuramoto was first to explore the collective behavior of oscillators through the lens of a dynamical phase transition controlled by the dimensionless ratio of the oscillators' frequency spread to their coupling strength [18]. This mean-field theory, which ignores network topology, predicts that at a critical coupling strength a subset of oscillators in a large system of attractively coupled oscillators will overcome differences in their intrinsic frequencies to oscillate with a common frequency and phase as a single, synchronized group or "cluster." The chemical reaction-diffusion networks in our study have differences and similarities with the Kuramoto model. One difference is that reaction-diffusion networks have short-range coupling instead of the all-to-all coupling of the Kuramoto model. Consequently, network topology influences their dynamics leading to spatiotemporal patterns, which are absent in the Kuramoto model. A similarity between the systems is that phase locking is destabilized when heterogeneity exceeds a critical value.

We experimentally study an oscillatory chemical reaction-diffusion network and examine its dynamics within the framework of symmetry-based network theories [11,19]. We use the well-characterized Belousov-Zhabotinsky reaction as the oscillatory medium, and embed it in a polydimethylsiloxane (PDMS) network patterned using soft lithography [20,21]. One significance of studying a self-contained reaction-diffusion system lies in the potential for fabrication of autonomous devices that organize their spatiotemporal dynamics through processes analogous to living systems. This experimental system oscillates stably in a single attractor state for up to 70 periods [21], which is an order of magnitude longer than reported in previous studies of living networks [5,22,23]. This provides confidence that observed steady states correspond to fixed points of the idealized system that we model theoretically, which assumes a steady supply of reactants and removal of by-products. The enhanced longevity of our experiments over prior work is especially important given that the experimental system is closed and existence of a truly stationary state, in the sense that the state lasts infinitely long, represents an idealization. We restrict our examination to a four-ring network that is predominantly coupled through inhibitory interactions. We find that this network is robustly multistable and exhibits dynamics that are captured by a phase model faithful to the Belousov-Zhabotinsky (BZ) chemistry. [24,25] that can be quantitatively fit to data with few, physically interpretable parameters. This network therefore serves as a minimal but rich model system for exploring the predictions of the H/K theorem and does so in a reaction-diffusion context that is important for biological phenomena [2,17].

By observing the dynamics of hundreds of instances of the four-ring network, which is an order of magnitude more experiments than done previously in reaction-diffusion networks [5,22,23], we are able to quantitatively compare spatiotemporal patterns in experiment to theory with and without heterogeneity. The BZ reaction exhibits dramatic changes in color due to the oxidation and reduction of the primary catalyst, ferroin. By tracking the color change, we identify the phase of each oscillator, which we then map to phase difference. This change of variables maps the periodic orbits of the system to fixed points in phase space. Theory predicts stability of all H/K-predicted fixed points for the homogeneous case of identical oscillators. This stability is attributed to features of the nonlinear function governing interactions between connected oscillators. By contrast, one H/K-predicted fixed point is absent in experimental observations and the remaining attractors are displaced and emerge as distributions in the ensemble. To quantify the degree of heterogeneity in our experiments, we fit the phase model to these data using the intrinsic frequency difference between oscillators and coupling strength as fitting parameters. It is our measurements on ensembles of hundreds of networks that allows the accumulation of sufficient statistics to classify observed attractors as belonging to idealized symmetric states, or as arising from heterogeneity.

By including the measured heterogeneity in our model we reproduce the experimentally observed distributions. We make sense of these distributions through a bifurcation analysis that shows that each attractor is destroyed at a different threshold of heterogeneity. Critically, this threshold depends on the spatial distribution of that heterogeneity, in distinction to the Kuramoto model. Despite this complexity, we find that this behavior can be understood semianalytically in a manner analogous to the Kuramoto model by examining dynamics and bifurcations along a few invariant manifolds provided by the H/K theorem. We show that hypotheses generated by idealized symmetry-based theories are relevant to experimental self-organized networks in which both the oscillators and coupling are fully chemical. We conclude that symmetry-based theories provide an essential scaffold for systematically building qualitative intuition and guiding quantitative analysis, even in a highly nonlinear and heterogeneous system.

II. METHODS

A. Experiment

We designed a reaction-diffusion network consisting of a ring of four diffusively coupled nanoliter volume batch reactors laid out in a square 2×2 lattice with nearest-neighbor coupling (Fig. 1). Previously, we employed emulsions containing the BZ oscillating reaction to study reaction-diffusion networks [24–31]. However, the diffusive coupling between surfactant stabilized emulsion drops was difficult to characterize, and flow rate fluctuations introduced compositional and geometric heterogeneity. Both contributed to a large degree of variability between experiments and precluded performing experiments on ensembles of hundreds of networks. Here, we improved reproducibility by manufacturing these reactors to high precision from elastomeric PDMS using soft lithography techniques adapted from semiconductor manufacturing and filled the reactors with the oscillatory BZ reaction as described previously [20,21], illustrated in Fig. 1 and in Appendix A.
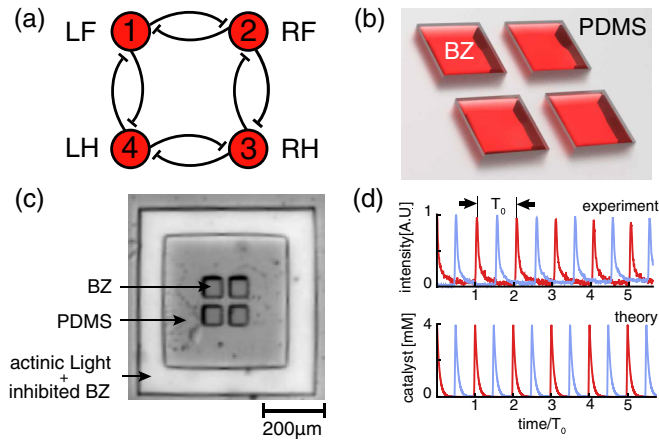
FIG. 1. (a) Schematic of a network of a ring of four inhibitory coupled oscillators. Indexing of nodes is indicated as either a number (1,2,3,4), or a leg of a quadruped (LF, RF, RH, LH) with L left, R right, F front, and H hind. (b) Schematic of the experimental system. The reactors are divots in the PDMS, filled with BZ and sealed between two glass plates. (c) Photograph of BZ-filled four-ring network. Light illuminates BZ in a channel surrounding the network, activating the photosensitive catalyst to provide a constant-chemical boundary condition. (d) Two adjacent reactors (red and blue traces) in the network oscillating 180° out of phase with each other. Top: Measured transmitted intensity versus time. Bottom: Simulated oxidized catalyst concentration (mM) versus time. In both, T_0 is the period at steady state of ~300 s in experiment and ~250 s in theory and is indicated by the two arrows.

We have previously shown that PDMS reacts with the BZ-produced bromine, which leads to a number of deleterious effects, such as a reduction in the number of cycles of oscillation before oscillations cease and an increase in the variation of oscillation period in an ensemble of oscillators [21,32]. These undesirable effects increased with increasing amounts of PDMS; thus, a key technical advance was reducing the amount of excess PDMS underneath each reactor to layers under 2 μm thickness (see Fig. S1(a) of the Supplemental Material [33]). To obtain a large statistical sample of trajectories we made devices that combined 9 or 16 copies of the 2×2 network [20] (Appendix A). To maximize homogeneity in the chemical concentrations of each of the reactors, we simultaneously filled the entire set of networks by pipetting a drop of BZ that floods all the reactors before sealing the sets of reactors by clamping the PDMS between two glass plates (see Figs. S1 and S2 or the Supplemental Material [33], and Supplementary Movies in Ref. [20]).

The chemical coupling between adjacent reactors arises from the permeation of chemical species through the intervening PDMS wall and mainly consists of bromine-induced inhibition, with a weaker activator coupling, perhaps by bromous acid and the bromine dioxide radical [20,24–28,30,31,34–38]. As PDMS reacts with bromine, it is important for the reactors to be separated by thin walls of PDMS to maintain chemical coupling. After mixing the BZ reagents, pipetting them onto the PDMS networks, sealing the networks, and placing the sample in the dark for an induction period of 20 min, it was observed that all reactors

began to oscillate and collectively form spatiotemporal patterns [Fig. 1(d)] [20]. We visualize the oxidation-reduction dynamics of the BZ reactors using a custom microscope described in the Supplemental Material [33]. To maximize contrast, we illuminate the wells with blue-green 515-nm light. In its reduced state, the ferroin catalyst is red and blocks the transmission of the light. Upon oxidation, the wells turn blue, which increases their transmission, allowing more light to reach a detector.

The reactors form a closed system and consequently the oscillators have a finite lifetime as the reactants are consumed and waste products accumulate. However, although the amplitude of the chemical oscillations decreases over time, the oscillators maintain a nearly constant period for a duration of order 70 oscillations [21]. Further, the response to light perturbations in this study remained predictable over this time period, suggesting that the phase-response curve of the chemistry was sufficiently steady. Based on this long-term stability, we assume that the underlying phase dynamics of the individual BZ oscillators remains constant during the duration of the experiment, thus allowing us to study phase relationships between reactors as they evolve over time (see Movies S1–S4 in the Supplemental Material [33]). Each four-ring network is isolated from the environment because the reactors are surrounded by a zone of photosensitive BZ that is held at constant chemical conditions by the application of actinic light [20]. We designed the wells to be small compared to the diffusive length scale so that we could assume the reactors to be well mixed in our model, e.g., $w < \sqrt{D\tau}$ with w the width of each square reactor ($w = 62\ \mu$m), D the diffusion constant of each BZ chemical ($D \sim 10^{-9}$ m^2 s^{-1}), and τ the duration of a BZ oscillation ($\tau \sim 300$ s).

B. Reaction-diffusion model

We model the dynamics of our oscillator network as a discrete reaction-diffusion system. The following describes the evolution of the chemical composition $\mathbf{c} = (x, y, z, u)$ of each node i due to intranodal reactions $\mathbf{R}(\mathbf{c}; \mathbf{K}) = (R_x, R_y, R_z, R_u)$ and internodal diffusive coupling $\propto \mu$:

$$\dot{\mathbf{c}}_i = \mathbf{R}(\mathbf{c}_i; \mathbf{K}_0) + \nabla_{\mathbf{K}} \mathbf{R}|_{\mathbf{K}_0} \delta \mathbf{K}_i + \sum_{j=1}^{4} A_{ij} \mu (\mathbf{c}_j - \mathbf{c}_i),$$

$$A_{ij} = \begin{bmatrix} 0 & 1 & 0 & 1 \\ 1 & 0 & 1 & 0 \\ 0 & 1 & 0 & 1 \\ 1 & 0 & 1 & 0 \end{bmatrix}, \quad \mu = \begin{bmatrix} k_e k & 0 & 0 & 0 \\ 0 & 0 & 0 & 0 \\ 0 & 0 & 0 & 0 \\ 0 & 0 & 0 & k \end{bmatrix}. \quad (1)$$

Dynamics within each node are governed the Vanag-Epstein (VE) model [34] of the Belousov-Zhabotinsky reaction, a four-species model where $x = $ [HBrO$_2$], $y = $ [Br$^-$], $z = $ [oxidized catalyst], and $u = $ [Br$_2$]:

$$R_x(x, y, z) = k_2 y - k_1 xy - 2k_3 x^2 + \frac{k_4 x(c_o - z)}{(c_o - z + c_{\min})},$$

$$R_y(x, y, z) = -2k_2 y + k_7 u + k_9 z - 3k_1 xy - k_3 x^2,$$

$$R_z(x, z) = -(k_9 + k_{10})z + 2\frac{k_4 x(c_o - z)}{(c_o - z + c_{\min})},$$

$$R_u(x, y, u) = k_2 y - k_7 u + 2k_1 xy + k_3 x^2. \quad (2)$$

A set of parameters and reaction rates $\mathbf{K} = (k_1, k_2, \ldots)$ controls the model, with $\mathbf{K}_0$ representing the average reactor composition, Table V shows the values used throughout. We allow for slight heterogeneity by expanding the reaction dynamics $\mathbf{R}$ about this mean composition; in Eq. (1) $\nabla_{\mathbf{K}}\mathbf{R}$ is the sensitivity or Jacobian of the reaction dynamics with respect the parameters and $\delta\mathbf{K}$ is a vector of small deviations from the mean composition. The assumption of small deviations allows us to readily incorporate heterogeneity into a phase model of the oscillator network that we will introduce in Sec. II C. Previous works on BZ networks have found it necessary to introduce small amounts of chemical heterogeneity in order to bring theory into agreement with experiment [25,28] and a recent study of single BZ oscillators in PDMS has further quantified variations in oscillator frequency [21]. In principle, our analysis could have included heterogeneity in coupling strength as well. However, in previous work, we found that relatively large volume disparities are needed to substantially shift the location of fixed points [25].

The matrix A is the adjacency matrix and encodes the four-ring topology. This matrix assumes no diagonal coupling between wells. We explored this possible contribution but found the quality of fit to be insensitive to the ratio of diagonal coupling to nearest-neighbor coupling over a plausible range of values (i.e., diagonal $<$ nearest-neighbor coupling). Connected reactors exchange species at a rate proportional to the difference in concentrations. The diagonal matrix μ dictates the species-dependent rates of this diffusive coupling. Our model therefore assumes that no reactions are present within the PDMS barriers. This is not the case and it has been shown that bromine reacts with PDMS in a complex manner [32]. We account for the removal of bromine due to reaction with PDMS by introducing fitting parameters k_e and k describing the chemical coupling between oscillators. We can neglect storage within the membrane due to the short separations between reactors $\mathcal{O}(10\,\mu\mathrm{m})$ (quasisteady assumption) [25,26]. As described in Sec. II A, PDMS is selectively permeable to apolar Br_2 (variable u in the VE model). Br_2 is therefore the dominant communicable species with coupling rate k. We additionally consider weak coupling through $HBrO_2$; the ratio between the two is governed by $k_e < 1$ and is determined by fitting to data. We examine the implications of these two different modes of coupling in Sec. II C.

C. Phase model

Since we are interested in studying phase-locking phenomena in the four-ring network, we now simplify our model through the method of phase reduction. We do so by parametrizing the time-dependent concentrations through the *phase* ϕ of the limit cycle oscillations exhibited by each reactor, as proposed by Winfree [39] and widely used in various studies of chemical and biological oscillators [18,25,40–43]. We assume that all oscillators share a common limit cycle with angular frequency ω_0, which is determined by the free-running (uncoupled) dynamics of $\mathbf{R}(\mathbf{c}, \mathbf{K}_0)$. The phase variable therefore naturally progresses linearly from zero to 2π when oscillators are uncoupled such that $\dot{\phi} = \omega_0$.

In this framework, the phases of each oscillator are mutually perturbed by diffusive coupling. The sensitivity of phase
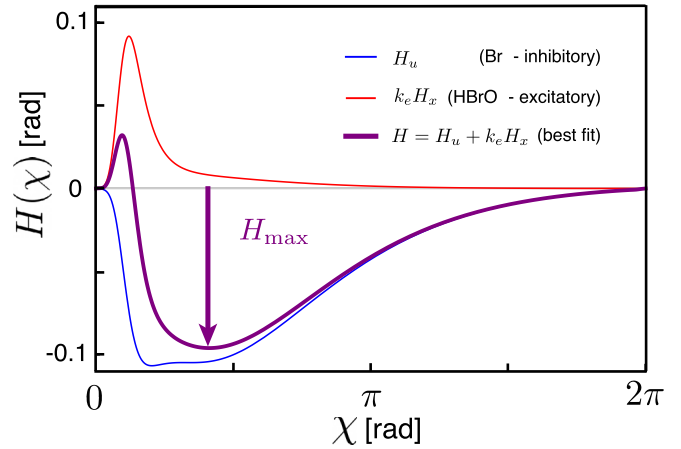

FIG. 2. The interaction functions of coupled BZ oscillators as a function of phase difference $\chi = \phi_j - \phi_i$. The sign indicates whether the interaction is phase advancing ($H > 0$) or phase delaying ($H < 0$). H_u (blue) is the interaction function due to Br_2 diffusion between reactors and H_x (red) is from $HBrO_2$. The total H (purple) is a weighted mix $H(\chi) = H_u(\chi) + k_e H_x(\chi)$, where $k_e = 0.05$ was determined by fitting time series data to Eq. (4). Since H_x is largely zero except for χ between zero and $\pi/2$, $k_e H_x$ adds a bump of phase advancing dynamics near zero, without affecting the otherwise phase delaying behavior of Br_2.

to the addition or removal of chemical species is determined by the infinitesimal phase-response curve (PRC), which we derive numerically from the VE model, Eq. (2) [44]. The PRC is subsequently used to calculate an interaction function H that encodes the impact on phase of one oscillator by another as a function of the relative phase between them. It is created by convolving the PRC with the diffusive flux between those connected oscillators. In the creation of H, we assume that the phase difference evolves slowly compared to the phase of each oscillator and that the oscillators return rapidly to their limit cycles after perturbations. Additional details are shown in Appendix C and Refs. [41,42,44].

For BZ-in-PDMS networks, we find through fitting to data that H has two contributions, each arising from the two communicable species such that $H = k_e H_x + H_u$. Figure 2 shows both functions and their combination with a best-fit ratio k_e. The interaction functions are signed differently because $HBrO_2$ (x) serves an excitatory role in the BZ chemistry and, when added to an oscillator, advances its phase. By contrast, Br_2 is rapidly converted to the inhibitor Br^- and delays the phase of oscillation. The phase dynamics of each oscillator are now given by

$$\dot{\phi}_i = \omega_0 + \left[\delta\omega_i + k\sum_{j=1}^{4} A_{ij}H(\phi_j - \phi_i)\right]. \quad (3)$$

Following Ref. [41], this framework also permits the influence of small deviations from the average composition of the oscillators, $\delta\mathbf{K}_i$ in Eq. (1), to show up as shifts in intrinsic frequency $\delta\omega_i$. Similar to the computation of H, each $\delta\omega_i$ is the period averaged convolution of the PRC with $\nabla_{\mathbf{K}}\mathbf{R}\delta\mathbf{K}_i$ as the forcing function instead of the diffusive flux. Since there
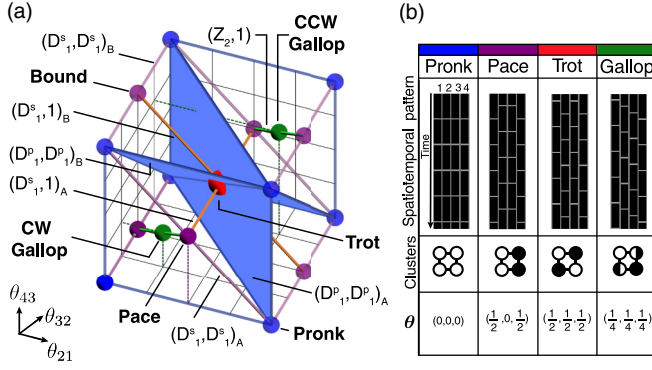
FIG. 3. (a) The eight categories of invariant manifolds for a network of four nodes with square symmetry predicted by the H/K theorem presented in the state space of phase differences is a periodic three-dimensional (3D) cube, $\theta_{ij} \in (0, 2\pi]$. There are four categories of phase-locked periodic states (points), three categories of lines, and one category of planes; each are colored according to their category in Table II. All linear and planar invariant are periodic; blue lines correspond to the edges of the planes. (b) The four point manifolds predicted by theory, Pronk, Pace/Bound, Trot, and Gallop, are represented (first row) as space-time plots, (second row) as networks with synchronized clusters indicated by color, and (third row) as a triplet of phase differences, $\boldsymbol{\theta}$, with units of fraction of a period.

are many possible $\delta\mathbf{K}$ that could lead to shifts in intrinsic frequency, we instead measure differences in intrinsic frequency between oscillators $\boldsymbol{\Delta\omega}$ by fitting to data; however, we note that the phase reduction formalism makes clear the connection between $\delta\omega$ and the original reaction-diffusion model.

In order to more readily analyze phase-locking behavior of the model and noting that the right hand side of Eq. (3) depends only on the phase *difference* of connected wells, we change variables from phase to phase difference. We arbitrarily choose the three phase differences $\boldsymbol{\theta} = (\theta_{21}, \theta_{32}, \theta_{43})$ as the new system variables, where $\theta_{ij} = \phi_i - \phi_j$, and rewrite the dynamics accordingly, where the heterogeneity of oscillators is similarly defined, $\Delta\omega_{ij} \equiv \delta\omega_i - \delta\omega_j$ and $\boldsymbol{\Delta\omega} \equiv (\Delta\omega_{21}, \Delta\omega_{32}, \Delta\omega_{43})$:

$$\dot{\theta}_{21} = \Delta\omega_{21} + k[H(\theta_{32}) + H(-\theta_{21}) - H(\theta_{21})$$
$$- H(\theta_{43} + \theta_{32} + \theta_{21})],$$
$$\dot{\theta}_{32} = \Delta\omega_{32} + k[H(\theta_{43}) + H(-\theta_{32}) - H(\theta_{32})$$
$$- H(-\theta_{21})],$$
$$\dot{\theta}_{43} = \Delta\omega_{43} + k[H(-(\theta_{43} + \theta_{32} + \theta_{21})) + H(-\theta_{43})$$
$$- H(\theta_{43}) - H(-\theta_{32})]. \quad (4)$$

For compactness, we refer to the system of equations (4) as $\dot{\boldsymbol{\theta}} = \boldsymbol{\Psi}(\boldsymbol{\theta}; \boldsymbol{\Delta\omega})$. As each of the phase differences is periodic on $(0, 2\pi]$, the new state space is a 3-torus. Although the 3-torus cannot be drawn in three dimensions, it is equivalent to a Cartesian cube with periodic boundaries, allowing visualization of the full dynamics [see Fig. 3(a)].

In summary, the reduced model in Eqs. (4) predicts the evolution of phase difference between oscillators as a function of the following parameters: (a) diffusive mass transfer coefficient k (s^{-1}), which scales the interaction function H (rad);

(b) coupling strength ratio k_e, which determines the shape of the H function in Fig. 2(a); and (c) differences in intrinsic frequency between oscillators, $\boldsymbol{\Delta\omega}$ (rads^{-1}).

D. H/K theorem

Symmetries place constraints on the behavior of dynamical systems. The impact of symmetries, once identified, is best understood through the concept of equivariance. A system is said to be γ equivariant under the symmetry operation γ when its dynamics f commute under the action of γ, such that $f(\gamma x) = \gamma f(x)$. This implies that if a system trajectory x' exists, so will $\gamma x'$.

For a given symmetry, there will also naturally exist a set of points in phase space that remain unchanged, $\gamma x = x$. The equivariance property then tells us that their dynamics must also remain the same, requiring that they be either trivially zero or tangent to the set of unchanged points. These special regions in phase space are known as invariant manifolds (IMs) because they are preserved by system dynamics (i.e., all trajectories that begin on IMs will remain so for all time). We will later show how analyzing the stability of these manifolds provides an organizing template for understanding the flows of the system in phase space.

In general, identifying all the symmetries of a large dynamical system is difficult. However, in dynamical networks composed of identical nodes, the system inherits spatial symmetries from the underlying network. Analyzing the network topology therefore readily yields a group of symmetries K that apply to the dynamics [7,11,12]. In the special case of oscillators, the temporal periodicity gives rise to an additional group H corresponding to phase shifts in the trajectory [11,15]. A group-theoretic result in this field called the H/K (or H mod K) theorem rigorously proves the existence of ordinary differential equation (ODE) systems that possess spatiotemporal patterns arising from the pair (H,K) [3,12,15]. The theorem does not guarantee a *given* ODE system will possess all patterns satisfying the theorem, but does provide a "catalog" of spatiotemporal patterns for which the system can be searched. For weakly coupled limit cycle oscillators, however, we are guaranteed an ODE system that possesses the necessary temporal symmetries because the interaction functions are time periodic by construction. This restricts us to patterns for which the oscillators possess identical periods, which is the focus of this work; however, there can be other spatiotemporal patterns for which periods are not identical [12].

The simplest example is a pair of identical oscillators, which is symmetric under the action of the group Z_2 that exchanges the nodes. The first solution guaranteed by the H/K theorem is in-phase synchrony, denoted (Z_2, Z_2). In this state both nodes are equal and can be interchanged by K = Z_2 with no change to the solution. The other solution is when the two oscillators are antiphase to one another, denoted $(Z_2, 1)$. The states of the nodes in this solution are never equal due to K = 1. However, the solution is unchanged by interchange of the nodes combined with a half-period shift in time by H = Z_2.

The required spatiotemporal and spatial symmetry solutions of the four-ring, or D_4 symmetric, system are periodic

TABLE I. Symmetry required invariant manifolds for an oscillator network possessing square or dihedral 4 (D_4) symmetry. D_4, all symmetries of a square; D_n^p, reflection across n diagonals; D_n^s, reflection across n, vertical or horizontal, axes; Z_4, 90° rotation; Z_2, 180° rotation; 1, no operation. The first four classes of manifolds are phase-locked states. The column marked "Phase" graphically indicates the spatiotemporal pattern with symbols representing the phase in percentage of a full cycle: white circle, 0%; white/black, 25%; black circle, 50%; black/white, 75%. The second four classes of manifolds are symmetrically clustered states, related by arbitrary phase shifts η_1, η_2 $\in (0, 2\pi]$. The graphical representation of nodes in the column "Phase" have solid, striped, or dot motifs. Different motifs are related by an arbitrary phase shift. Similar motifs with opposite background colors are antiphase with each other.

		Point invariant manifolds:			
Name **(H,K)**	**Phase**	$\mathbf{c_1}$	$\mathbf{c_2}$	$\mathbf{c_3}$	$\mathbf{c_4}$
Pronk (D_4, D_4)		$\mathbf{c}(\phi)$	$\mathbf{c}(\phi)$	$\mathbf{c}(\phi)$	$\mathbf{c}(\phi)$
Trot (D_4, D_2^p)		$\mathbf{c}(\phi)$	$\mathbf{c}(\phi + \pi)$	$\mathbf{c}(\phi)$	$\mathbf{c}(\phi + \pi)$
Pace $(D_2^s, D_1^s)_A$		$\mathbf{c}(\phi)$	$\mathbf{c}(\phi + \pi)$	$\mathbf{c}(\phi + \pi)$	$\mathbf{c}(\phi)$
Bound $(D_2^s, D_1^s)_B$		$\mathbf{c}(\phi)$	$\mathbf{c}(\phi)$	$\mathbf{c}(\phi + \pi)$	$\mathbf{c}(\phi + \pi)$
CW Gallop $(Z_4, 1)_A$		$\mathbf{c}(\phi)$	$\mathbf{c}(\phi + \frac{\pi}{2})$	$\mathbf{c}(\phi + \pi)$	$\mathbf{c}(\phi + \frac{3\pi}{2})$
CCW Gallop $(Z_4, 1)_B$		$\mathbf{c}(\phi)$	$\mathbf{c}(\phi + \frac{3\pi}{2})$	$\mathbf{c}(\phi + \pi)$	$\mathbf{c}(\phi + \frac{\pi}{2})$
		Linear invariant manifolds:			
$(D_1^s, D_1^s)_A$		$\mathbf{c}(\phi)$	$\mathbf{c}(\phi + \eta_1)$	$\mathbf{c}(\phi + \eta_1)$	$\mathbf{c}(\phi)$
$(D_1^s, D_1^s)_B$		$\mathbf{c}(\phi)$	$\mathbf{c}(\phi)$	$\mathbf{c}(\phi + \eta_1)$	$\mathbf{c}(\phi + \eta_1)$
$(D_1^s, 1)_A$		$\mathbf{c}(\phi)$	$\mathbf{c}(\phi + \pi)$	$\mathbf{c}(\phi + \eta_1)$	$\mathbf{c}(\phi + \eta_1 + \pi)$
$(D_1^s, 1)_B$		$\mathbf{c}(\phi)$	$\mathbf{c}(\phi + \eta_1 + \pi)$	$\mathbf{c}(\phi + \eta_1)$	$\mathbf{c}(\phi + \pi)$
$(Z_2, 1)$		$\mathbf{c}(\phi)$	$\mathbf{c}(\phi + \eta_1)$	$\mathbf{c}(\phi + \pi)$	$\mathbf{c}(\phi + \eta_1 + \pi)$
		Planar invariant manifolds:			
$(D_1^p, D_1^p)_A$		$\mathbf{c}(\phi)$	$\mathbf{c}(\phi + \eta_1)$	$\mathbf{c}(\phi)$	$\mathbf{c}(\phi + \eta_2)$
$(D_1^p, D_1^p)_B$		$\mathbf{c}(\phi)$	$\mathbf{c}(\phi + \eta_1)$	$\mathbf{c}(\phi + \eta_2)$	$\mathbf{c}(\phi + \eta_1)$

invariant manifolds, subspaces in which the dynamics remain confined. Although the theory is more general, we restrict ourselves to the case in which all the nodes are on the same limit cycle, as this corresponds to the phase-locked attractors observed in the experiment. With this assumption the H/K theorem guarantees that any system of four oscillators with square symmetry will possess eight categories of invariant manifolds with varying dimensionality [12]. These states are readily described in terms of their phase relationships between pairs, defined as the fraction of a period they are shifted from each other on their common limit cycle (see Table I). Of the eight categories, four are phase locked, with fixed phase relationships among the nodes, three possess one degree of freedom, and one possesses two degrees of freedom in their phase relationships, as enumerated in Table I.

TABLE II. Symmetry required invariant manifolds parametrized by relative phases η_1, η_2, which vary from zero to 2π. All representations, modulo 2π, are shown.

	Point invariant manifolds:	
Name	Phase	$(\theta_{21}, \theta_{32}, \theta_{43})$
Pronk		$(0, 0, 0)$
Trot		(π, π, π)
Pace Bound		$(\pi, 0, -\pi)$ $(0, \pi, 0)$
CW Gallop		$\left(\frac{\pi}{2}, \frac{\pi}{2}, \frac{\pi}{2}\right)$
CCW Gallop		$\left(-\frac{\pi}{2}, -\frac{\pi}{2}, -\frac{\pi}{2}\right)$
	Linear invariant manifolds:	
$(D_1^s, D_1^s)_A$		$(\eta_1, 0, -\eta_1)$
$(D_1^s, D_1^s)_B$		$(0, \eta_1, 0)$
$(D_1^s, 1)_A$		(π, η_1, π)
$(D_1^s, 1)_B$		$(\eta_1, \pi, -\eta_1)$
$(Z_2, 1)$		$(\eta_1, \pi - \eta_1, \eta_1)$
	Planar invariant manifolds:	
$(D_1^p, D_1^p)_A$		$(-\eta_1, \eta_1, \eta_2)$
$(D_1^p, D_1^p)_B$		$(\eta_1, \eta_2, -\eta_2)$

The varying dimensionality of the invariant manifolds becomes transparent when representing them in the phase difference space of our model in Eqs. (4). In this coordinate system, the invariant manifolds are simple, geometric objects: points, lines, and planes, enumerated in Table II. This transformation enables the consequences of the H/K theorem on the dynamics in state space to be visualized in a way that would be impossible in the full chemical model, Eq. (1).

The four categories of point invariant manifolds find six representations in phase space. Each can be identified with gaits of quadrupeds and are enumerated in Table I, and visualized in Fig. 3(b). The first two categories are *Pronk*, in which all the legs advance simultaneously, and *Trot*, for which diagonal legs are in phase, and the two diagonal pairs of legs are half a period out of phase. *Pace* and *Bound* form one category. In Pace, legs on each side are in phase and opposite sides out of phase, while for Bound, legs on opposite sides are in phase and the front legs out of phase with the hind legs. We give them distinct names in order to make contact with quadruped gaits but because they are essentially identical (related through a 90° rotation), we refer to them interchangeably in the remainder of the text. *Clockwise* (*Counter Clockwise*) *Gallop* is another category in which the legs advance in a clockwise (counterclockwise) manner with each leg advancing a quarter of a period later than the preceding leg.

The remaining four categories are higher-dimensional invariant manifolds (lines or planes) containing trajectories that maintain a subset of the H/K-predicted symmetries. Along one-dimensional (1D) invariant manifolds, the network can
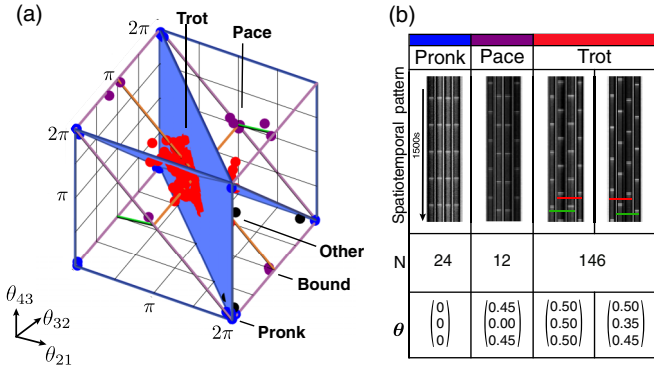
FIG. 4. (a) Experimental phase-locked states plotted within state space. There are three characteristic distributions, associated with the Pronk, Pace/Bound, and Trot states. They are colored to reflect which H/K state they are affiliated with as in Fig. 3, using a state-specific cutoff determined by simulations detailed later in Appendix G. (b) First row: Example space-time plots of steady states in (a). Due to the wide dispersion of the Trot distribution, different states within the Trot distribution can appear qualitatively different; the last column shows one such example. Second row: The number of times a state is observed. Third row: Measured phase difference. Videos of experiments shown in Movies S1–S4 of the Supplemental Material [33].

be split into two pairs of reactors, such that within pairs the reactors are in phase or antiphase, while between pairs reactors have an arbitrary phase shift. Along two-dimensional manifolds, two nodes must oscillate in phase while the other two nodes are at arbitrary phase shifts. These invariant manifolds intersect throughout phase space. For example, the two-dimensional manifolds intersect the one-dimensional manifolds, and the 1D manifolds intersect the phase-locked zero-dimensional manifolds [Fig. 3(a)]. The same manifolds are plotted alongside experimental data in Fig. 4.

The H/K theorem predicts the existence of these invariants; however, it neither prescribes their stability nor precludes the existence of others. To address questions of stability, we use our specific model of the oscillators and their interactions.

III. RESULTS

A. H/K and homogeneous phase model predictions

Using the H/K theorem's predictions as a jumping off point, we first examine the stability of D_4's invariant manifolds in the phase model, Eqs. (4). As discussed above, in phase-difference space, the invariant manifolds with no degrees of freedom—Pronk, Bound, Trot, and Gallop—are steady states rather than high-dimensional limit cycles. Linear stability analysis reveals that the system in Eqs. (4) is multistable, with each one of the point H/K manifolds forming a competing attractor.

We briefly demonstrate the analysis here; further details are in Appendix E. We first compute the Jacobian of the system, $J(\boldsymbol{\theta}) = \nabla_{\boldsymbol{\theta}} \Psi(\boldsymbol{\theta})$. The steady states that satisfy $\Psi(\boldsymbol{\theta}^{\dagger}) = 0$ are then linearly stable provided the real

components of the eigenvalues λ of $J(\boldsymbol{\theta}^{\dagger})$ are negative. Conveniently, multiple attractors lie on the line so we consider $\boldsymbol{\theta}_{\eta} = (\eta, \eta, \eta)$. This line includes Pronk ($\eta = 0$), Gallop ($\eta = \pi/2$), and Trot ($\eta = \pi$). The eigenvalues for these three cases are then $\lambda = \{-2(H'(\eta) + H'(-\eta)), -(H'(\eta) + H'(-\eta)) \pm i(H'(\eta) - H'(-\eta))\}$. The stability of each is therefore governed by the sign of a single quantity $H'(\eta) + H'(-\eta)$. From the plot of the H function in Fig. 2, we see that $H'(\eta) > 0$ for $\eta = 0, \pi/2$, and π, so the eigenvalues are negative. Similarly, the conditions for the stability of Bound/Pace rely on H having positive slope at both zero and π, which it does. Consequently, the system will converge to at least these four states depending upon initial condition. By contrast, in the Kuramoto case $H \sim \sin()$, Trot would be an attractor, Pronk a repeller, Pace/Bound a saddle, and Gallop a neutrally stable fixed point [45].

Simulations initiated from an exhaustive set of $\sim 10^5$ initial conditions further show that each initial condition flows to one of these phase-locked attractors [Figs. 5(a) and 5(b)], indicating that there are no other attractors besides the point invariant manifolds predicted by the H/K theorem. We numerically determined the basins of attraction of each attractor by dividing the 3-torus into a fine grid and identifying each initial point with the attractor to which it flowed, as shown in Figs. 5(a) and 5(b). The Pronk, Bound, and Gallop basins are smooth, closed volumes while the Trot basin fills the rest of the state space [Fig. 5(b)]. The state with the largest basin of attraction is Trot, followed by Gallop, Bound, and Pronk. The attraction basin of the Bound state is anisotropic and aligned with the (D_1^s, D_1^s) invariant manifolds [Figs. 5(a) and 6(a)]. Figures 5(a) and 6(b) reveal that trajectories remain near the (D_1^p, D_1^p) invariant manifolds as they flow to Trot. We find the convergence time to these attractors, approximated as the reciprocal of the maximum real eigenvalue of the attractor, are within experimentally relevant time frames. The convergence times, as measured in oscillation periods, for each attractor are 2.8 for Trot, 6.0 for Gallop, and 19.0 for both Bound and Pronk. In addition to these attractors, a direct numerical search for all roots of Eqs. (4), $\Psi(\boldsymbol{\theta}^{\dagger}) = 0$, revealed many additional steady states (158 saddle points and 4 repellers) that give further structure to the state space. All states are enumerated in Table SI and plotted in Fig. S6 of the Supplemental Material [33].

Theory predicts that the network's trajectories flowing towards its attractors are constrained and shaped by higher-order invariant manifolds [Fig. 6(a)]. To further quantify how the 1D and two-dimensional (2D) manifolds guide and structure dynamics, we calculate their transverse stability. We do so by leveraging the simple geometric forms of the invariant manifolds and the phase model in Eqs. (4) to perform a coordinate transformation that decomposes the dynamics into components tangent and normal to the manifolds. Details of this linear stability analysis are shown in Appendix E and Table SII in the Supplemental Material [33]. We find that the majority of the (D_1^s, D_1^s) and (D_1^p, D_1^p) manifolds are attracting; this causes nearby trajectories to collapse and remain on them (Fig. 6). The manifolds also exhibit small regions of repulsion that contain saddle nodes and demarcate separatrices. In this way, the theory combines the restrictions of symmetry and the unique system dynamics to predict both the basins of
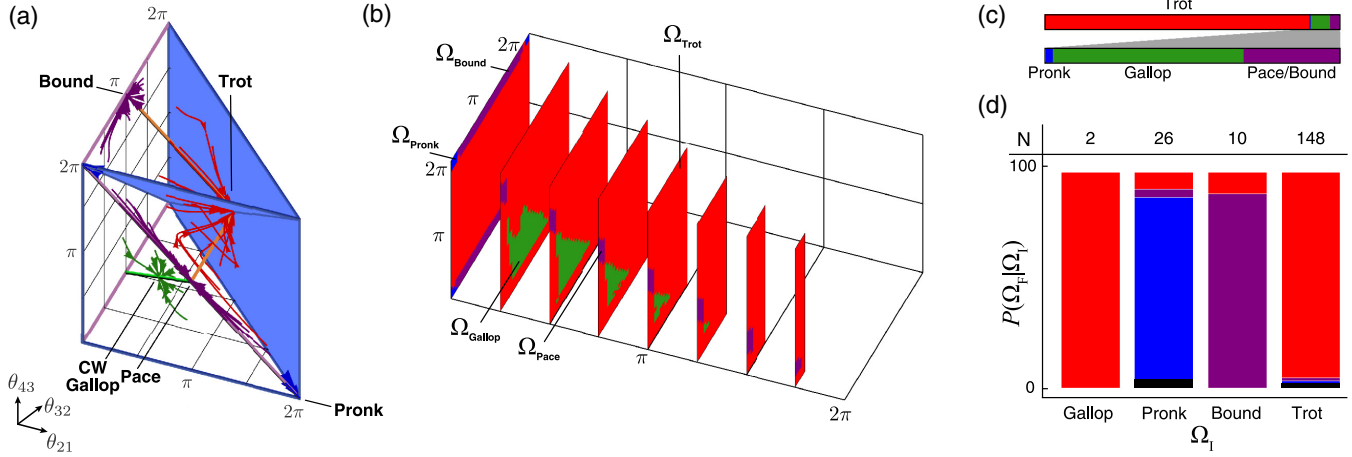
FIG. 5. Basins of attraction. States are labeled as in Fig. 3. (a) Simulations of Eqs. (4) show that all trajectories converge to the H/K-predicted attractors (point invariant manifolds), Pronk/Bound, Gallop, or Trot, depending on initial condition. Video of different perspectives in three dimensions is shown in Movie S5 [33]. The corresponding plot of all experiments is shown in Movie S6 [33]. (b) Basins of attraction of homogeneous model. The phase space is divided into regions Ω colored by the attractor to which all initial conditions in that set of points converges. (c) A dense, uniform sampling of initial conditions shows 89.9% go to Trot, 6.56% to Rotary Gallop, 3.33% to Bound/Pace, and 0.231% to Pronk. (d) The probability $P(\Omega_F|\Omega_I)$ that an experiment, which began in a theoretical basin Ω_I, converges to an attractor in region Ω_F. We list the number of observations, N, in the row above the chart. The plot shows that initial conditions for gallop were rarely accessible experimentally and did not converge to gallop. In contrast, of the 148 states initially in the theoretical Trot basin, 95.3% converged to that attractor. Of the remaining 4.7%, 1.35% went to Pronk, 1.35% went to Bound/Pace, and 2.03% went to Other.

attraction of the attractors and the symmetric, clustered transient transitions along the linear and planar invariant manifolds that connect the attractors. We note that the H/K theorem does not preclude the existence of other invariant manifolds. In fact, near the Gallop attractor, we observe trajectories coalescing onto a 2D surface [Fig. 5(a)].

B. Experimental observations of dynamics

To compare H/K and phase model predictions with experiment, we mapped the transmitted light intensity shown in Fig. 1(d) to phase by attributing the time of a reactor's peak oxidation to $\phi = 2\pi$ and linearly interpolating between
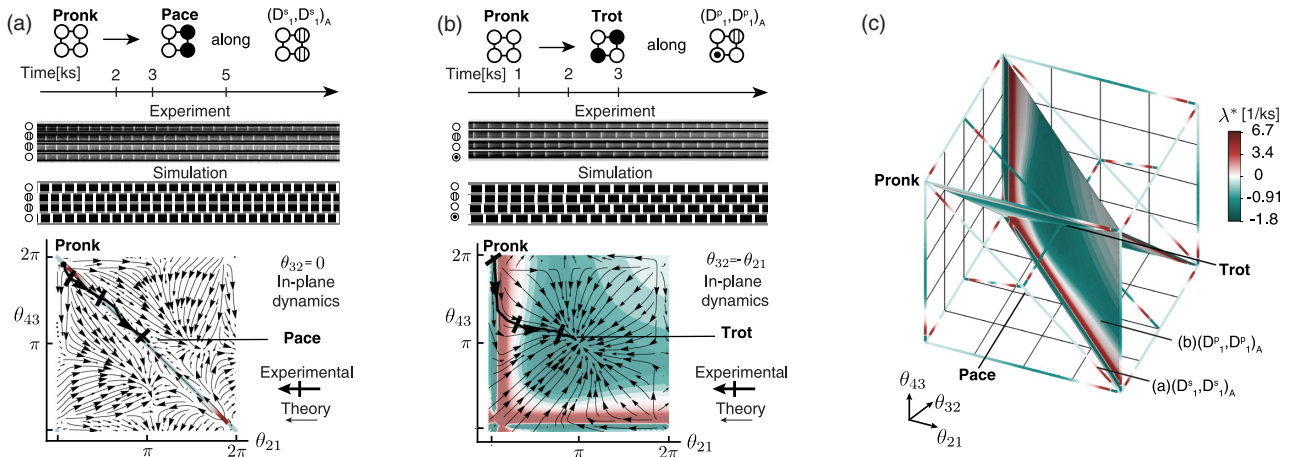

FIG. 6. Dynamics along higher-order H/K invariant manifolds in experiment and simulation. (a) Space-time plots from an experiment and simulation with a near-Pronk initial state transitioning to Pace. States form two symmetric clusters corresponding to the $(D_1^s, D_1^s)_A$ invariant manifold. In the lower panel the experimental trajectory is shown as an arrow traveling through a 2D slice of state-space superimposed over the theoretical velocity field. Video of experiment synchronized to progression along space-time plot and trajectory in state-space is shown in Movie S8 [33]. (b) Space-time plots from an experiment and simulation with a near-Pronk initial state transitioning to Trot. The transition corresponds to the $(D_1^p, D_1^p)_A$ invariant manifold. Video of experiment synchronized to progression along space-time plot and trajectory in state-space shown in Movie S9 [33]. (c) The invariant manifold surfaces attract or repel in a state-dependent manner given by the computed maximum transverse eigenvalues λ^*. When positive (negative), nearby trajectories are repelled (attracted) from (to) the invariant manifold. Both the 2D $(D_1^p, D_1^p)_A$ and 1D $(D_1^s, D_1^s)_A$ invariant manifolds are largely attracting. Video of 3D perspective of plot is shown in Movie S10 [33].

these peaks. We subsequently calculated the three phase differences $(\theta_{21}, \theta_{32}, \theta_{43})$. We conducted 318 experiments of which 186, or 58%, phase locked following criteria defined in Appendix B. The complex, non-phase-locking trajectories were not analyzed beyond plotting a histogram of their phase differences over time in Fig. S5 of the Supplemental Material [33]; the following examines the dynamics of the phase-locked cases.

We first compare the phase-locked steady states observed in experiment to theory. We do so by plotting the phase differences at steady state in the 3D state space of the system [Fig. 4(a)]. We find clusters of steady states around three of the four attractors predicted by theory: Pronk (blue), Bound/Pace (purple), and Trot (red) [Fig. 4(a)]. The distributions around Pronk and Bound/Pace are tightly centered. Consequently, space-time plots of their spatiotemporal dynamics [Fig. 4(b)] are visually indistinguishable from the Bound and Pronk states in theory [Fig. 3(b)].

In contrast, the Trot-centered distribution is more diffuse. At its furthest extent, the spatiotemporal dynamics no longer qualitatively resemble the symmetry-predicted dynamics, as exemplified in Fig. 4(b), which presented a challenge in classifying the observed phase-locked states. To classify these states, it was necessary to perform hundreds of trials to accumulate enough statistics to recognize that attractors formed clouds of points distributed around the symmetry-predicted states. To help with the classification, we also performed simulations to be discussed more fully in Sec. III C. Briefly, simulations show that the region of the Trot attractor expands substantially in response to heterogeneity. We determine the bounds of this region for Trot, and the other attractors, through both large scale computation and bifurcation analysis. We then use the extent of those regions to classify our experimental data. We find that nearly all of the points distributed around Trot are instances of the original attractor subject to heterogeneity.

Finally, we did not observe the theoretically predicted Gallop attractors. Instead, the region of state space where we would expect Gallop is completely empty [Fig. 4(a)]. This indicates Gallop is either unstable or absent altogether. Like Trot, we will explain this discrepancy between theory and observation further in Sec. III C.

We can further assess the agreement between theory and experiment by examining the correspondence between initial condition and steady state. The theoretical plot of the basins of attraction summarizes this relationship by mapping each point in phase space to an attractor [Fig. 5(b)]. Experimental initial conditions were explored by applying phase-shifting perturbations to the networks at the beginning of the experiment using the method described in Ref. [29] and Appendix A. To compare, we plot the observed probability of converging to each attractor given the initial condition's basin [Fig. 5(c)]. Nearly all experiments that began in the theory-predicted basin flowed to the corresponding attractor. The exception was Gallop; trajectories that began in that basin flowed instead to Trot. We found this basin difficult to sample experimentally, so it is difficult to prove its existence or absence based on these observations alone. In the next section we discuss simulations incorporating heterogeneity that shed some light on these observations.

Finally, we look for evidence of the higher-order IMs in our experiment. Since theory predicts the transverse dynamics of the (D_1^s, D_1^s) and (D_1^p, D_1^p) manifolds to be largely attracting, we expect them to be observable. Strikingly, we find trajectories on these manifolds and, in the case of (D_1^p, D_1^p), find the trajectories to qualitatively match theory in that plane [Figs. 6(a) and 6(b)].

C. Heterogeneous phase model and bifurcation analysis

We hypothesized that the two main discrepancies between theory and experiment (the absence of gallop and the large cloud of steady states around trot) can be explained by allowing for heterogeneity in the intrinsic frequencies of Eqs. (4). We tested this by first measuring the degree of heterogeneity by fitting Eqs. (4) to experimental data with intrinsic frequency difference $\Delta\omega$, coupling strength k, and inhibitory-excitatory ratio k_e as fitting parameters (details are presented in Appendix C). We report the outcome as a distribution of dimensionless frequency differences $\overline{\Delta\omega} = \Delta\omega/(kH_{\max})$, where $\Delta\omega$ is scaled, both by the coupling strength k and the maximum amplitude of the interaction function, $H_{\max}$. We introduce the latter to facilitate comparison with the Kuramoto canonical case of sinusoidally coupled oscillators, for which the interaction function has unit amplitude (Fig. 7). We anticipate qualitative changes in dynamics when the heterogeneity exceeds the "height" of the interaction function [18,46]. We find that the distribution of $\overline{\Delta\omega}$ is approximately Laplacian with scale parameter $b = 0.244$ or standard deviation $\sigma = \sqrt{2} \times 0.244$ (Fig. 7). Previous work measured the distribution of intrinsic frequencies of isolated wells in the same BZ-in-PDMS system to have a 3% coefficient of variation [21]. This variation was attributed to slight differences in chemical concentration and boundary conditions created by the applied blue light [47]. By nondimensionalizing, we see that this small degree of heterogeneity is influential because the coupling is sufficiently weak. Figure 7(c) shows the fraction of experiments that possess a given overall heterogeneity $|\Delta\omega|$ or less (i.e., while the mean of ω_{ij} is zero, we find that it is unlikely that all frequency differences in a network will be zero). We subsequently incorporated heterogeneity into simulation by sampling from this distribution multiple times for each initial condition.

Figure 8(a) shows the resulting steady states in state space. The simulations produce a distribution of steady states with multiple clusters, four of which are centered about the expected H/K attractors. Qualitatively, the spatial extent of each is distinct. For example, Pronk is narrow while Trot is dispersed. We associate a steady state with an H/K attractor if it is within an attractor-specific cutoff distance determined by examining the density of steady states as a function of distance from an attractor. Steady states beyond the cutoff distances for all H/K attractors are classified as "Other" (Appendix G).

In comparing identified H/K steady states in heterogeneous simulations to those in homogeneous ($\Delta\omega = 0$) simulations, we see marked changes in the relative occurrences of each H/K state. The added heterogeneity dramatically reduced the presence of Gallop. Homogeneous simulations predicted that 6.0% ($N = 5399$) of trajectories would converge to Gallop, compared to 0.259% ($N = 34\,713$)
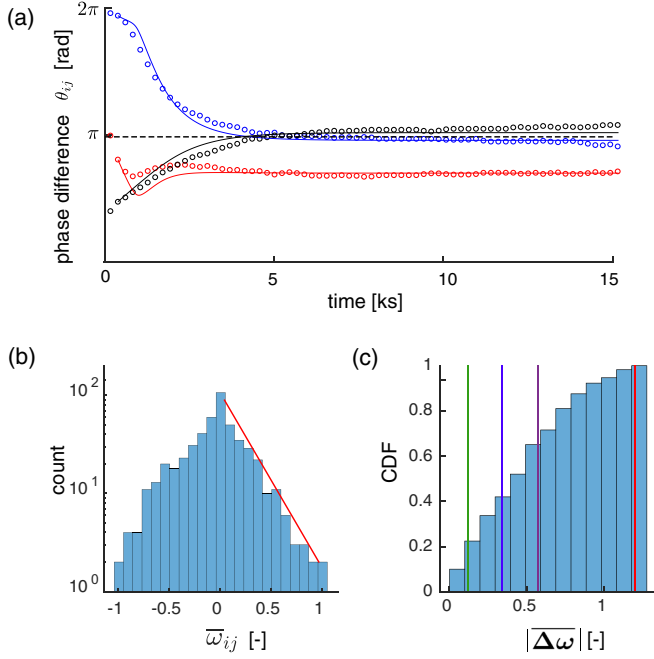
FIG. 7. (a) Example experimental trajectory converging to steady state (circles), and best-fit phase model (solid line). The fit model required heterogeneity $\overline{\Delta\omega}_{ij} \neq 0$ to fit data. For comparison, the steady-state phase difference $\boldsymbol{\theta}^{\dagger} = (\pi, \pi, \pi)$ of the homogeneous phase model is shown (dashed horizontal line). (b) Distribution of best-fit dimensionless intrinsic frequency differences $\overline{\Delta\omega} = \Delta\omega/kH_{\max}$, nondimensionalized by the coupling rate k and amplitude of the interaction function $H_{\max}$ (Fig. 2). The distribution is approximately Laplacian with scale factor $b = 0.2441$. (c) Cumulative probability distribution of $|\overline{\Delta\omega}|$ from (a). Lines denote the average heterogeneity $\langle|\overline{\Delta\omega}^{*}|\rangle$ at which the bifurcation analysis predicts the attractors: Gallop (green), Pronk (blue), Pace/Bound (purple), and Trot (red) will lose stability (Table III). This predicts the fraction of experiments that can support a given attractor given the inherent heterogeneity.

in heterogeneous simulations, a 23-fold decrease. In experiment this drops to 0% ($N = 186$). In contrast, Bound/Pace and Pronk experience, respectively, 2.1- and 3.2-fold decreases and Trot experiences a 1.1-fold increase through the elimination of Gallop. The share of steady states classified as Other is 3.43% in heterogeneous simulations, comparable to the 2.15% observed in experiments. It is unclear whether all the Other states should be classified as new states generated by frequency heterogeneity, or as states that are improperly classified according to the criteria described in Appendix G. However, we note the creation of new fixed points when heterogeneity is introduced. These new steady states appear as clusters labeled Other in Fig. 8 but are not associated with any of the H/K attractors. Numerical continuation of Pronk confirms the creation of a new fixed point at finite heterogeneity, but we did not explore its properties in detail. Finally, heterogeneous simulations recreate the observed cloud of steady states around Trot. Of the simulations that phase locked, we observed that those with the largest heterogeneity tended to exhibit increased convergence time, as is generically expected near a saddle node on an invariant circle bifurcation [46].

TABLE III. Summary of bifurcation analysis. Different patterns of heterogeneity $\boldsymbol{\Delta\omega} = \alpha\mathbf{W}$ are considered for positive and negative values of α. The second column shows the corresponding spatial distribution of intrinsic frequencies; nodes with identical colors have identical frequencies. The critical values are reported as the dimensionless ordered pair $[\bar{\alpha}_{+}^{*}, |\bar{\alpha}_{-}^{*}|]$, where $\bar{\alpha} = \alpha/(kH_{\max})$. The final row reports the average, dimensionless heterogeneity $\langle|\overline{\boldsymbol{\Delta\omega}}^{*}|\rangle$ at which bifurcations occur.

$\mathbf{W}$	ω	pronk	trot	pace	bound	CW	CCW
$\begin{bmatrix}1\\-1\\0\end{bmatrix}$		$\begin{bmatrix}0.35\\0.68\end{bmatrix}$	$\begin{bmatrix}1.4\\1.2\end{bmatrix}$	$\begin{bmatrix}0.42\\0.40\end{bmatrix}$	$\begin{bmatrix}0.42\\0.40\end{bmatrix}$	$\begin{bmatrix}0.089\\0.14\end{bmatrix}$	$\begin{bmatrix}0.089\\0.14\end{bmatrix}$
$\begin{bmatrix}1\\-1\\1\end{bmatrix}$		$\begin{bmatrix}0.7\\0.7\end{bmatrix}$	$\begin{bmatrix}1.9\\1.9\end{bmatrix}$	$\begin{bmatrix}0.55\\0.55\end{bmatrix}$	$\begin{bmatrix}0.55\\0.55\end{bmatrix}$	$\begin{bmatrix}0.18\\0.18\end{bmatrix}$	$\begin{bmatrix}0.18\\0.18\end{bmatrix}$
$\begin{bmatrix}1\\0\\-1\end{bmatrix}$		$\begin{bmatrix}0.35\\0.35\end{bmatrix}$	$\begin{bmatrix}0.93\\0.93\end{bmatrix}$	$\begin{bmatrix}0.93\\0.93\end{bmatrix}$	$\begin{bmatrix}0.35\\0.35\end{bmatrix}$	$\begin{bmatrix}0.083\\0.083\end{bmatrix}$	$\begin{bmatrix}0.083\\0.083\end{bmatrix}$
$\begin{bmatrix}0\\1\\0\end{bmatrix}$		$\begin{bmatrix}0.35\\0.35\end{bmatrix}$	$\begin{bmatrix}0.93\\0.93\end{bmatrix}$	$\begin{bmatrix}0.35\\0.35\end{bmatrix}$	$\begin{bmatrix}0.93\\0.93\end{bmatrix}$	$\begin{bmatrix}0.083\\0.083\end{bmatrix}$	$\begin{bmatrix}0.083\\0.083\end{bmatrix}$
$\begin{bmatrix}1\\1\\1\end{bmatrix}$		$\begin{bmatrix}0.12\\0.12\end{bmatrix}$	$\begin{bmatrix}0.40\\0.40\end{bmatrix}$	$\begin{bmatrix}0.13\\0.13\end{bmatrix}$	$\begin{bmatrix}0.42\\0.42\end{bmatrix}$	$\begin{bmatrix}0.032\\0.062\end{bmatrix}$	$\begin{bmatrix}0.062\\0.032\end{bmatrix}$
$\langle|\overline{\boldsymbol{\Delta\omega}}^{*}|\rangle$		0.34	1.2	0.57		0.12	

To gain a more quantitative understanding of each attractor's response to heterogeneity, we examined the response to frequency heterogeneity through a bifurcation analysis. Since we have three potential bifurcation parameters, $\boldsymbol{\Delta\omega} = (\Delta\omega_{21}, \Delta\omega_{32}, \Delta\omega_{43})$, we chose a representative subset of possible directions $\mathbf{W}$ with symmetries inspired by D_4 such that $\boldsymbol{\Delta\omega} = \alpha\mathbf{W}$; Fig. 8(b) shows the directions considered. These directions either break or coincide with the point symmetry of the attractors. We will show that the selection of directions we chose covers the most extreme cases, providing a framework for understanding the overall sensitivity of an attractor. Numerical continuation is used to identify the location of the system's attractors $\boldsymbol{\theta}^{\dagger}(\alpha)$ as α is varied. The critical values α^{*} at which stability is lost are reported in Table III for the system's attractors. All critical values are reported in dimensionless terms using $H_{\max}k$ as the scale (Fig. 2). We also summarize Table III's content graphically by plotting the points at which attractors are eliminated or lose stability through bifurcations $\boldsymbol{\theta}^{\dagger}(\alpha^{*})$ and connecting these points to form closed surfaces; the average magnitude of heterogeneity $\langle\overline{\boldsymbol{\Delta\omega}}^{*}\rangle$ reported measures the overall robustness of each attractor to heterogeneity [Fig. 8(c)]. In all cases, we find that a finite amount of heterogeneity is needed to eliminate the attractor; thus, all attractors are structurally stable. Notably, the average heterogeneity needed to eliminate Gallop is exceeded during $\sim$80% of experiments [Fig. 7(c)].

This analysis reveals important qualitative differences between the attractors as well. The critical values α^{*} at which
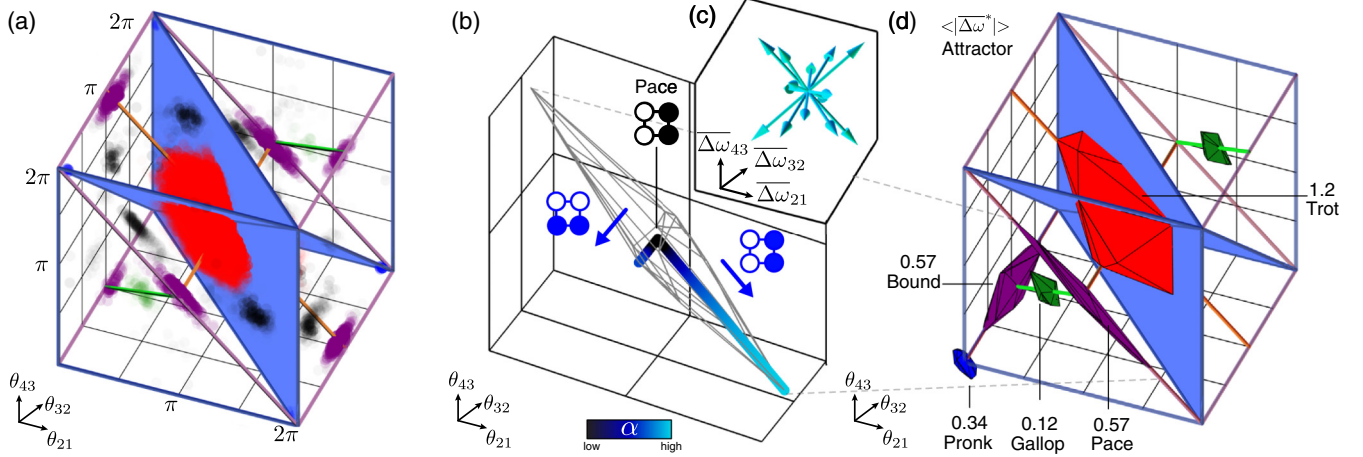
FIG. 8. (a) Phase-locked steady states of simulations with heterogeneity $\boldsymbol{\Delta\omega}$ sampled from the experimentally measured distribution (Fig. 7). The steady states are unimodally distributed about each H/K attractor. We associate a steady state with an attractor if they are within ones of these distributions or as "Other" (black) (Appendix G). Compared to homogeneous simulations, occurrence of Gallop is reduced by a factor of 23.5 and Trot becomes dispersed over a large volume (Fig. 5). Videos of 3D perspectives of plots are shown in Movies S11 and S12, respectively, in the Supplemental Material [33]. (b) Paths traced out by the Pace attractor in response to two patterns of heterogeneity indicated by the blue glyphs. Each pattern moves Pace along a different linear invariant manifold. The mesh surface shows the volume explored by Pace for all perturbations that we consider. (c) Schematic of all directions in heterogeneity $\mathbf{W}$ used during bifurcation analysis. (d) Surfaces of the phase differences $\boldsymbol{\theta}^\dagger$ at which an H/K attractor loses stability due to a heterogeneity induced bifurcation. These surfaces bound distributions of steady states in (a). The surfaces are labeled by the average magnitude of heterogeneity $\langle|\overline{\boldsymbol{\Delta\omega}}^*|\rangle$ at which loss of stability occurs. Note that the surfaces have phase differences below zero, as the surfaces are centered about points containing zero values. As a result, the surfaces about Pronk, Bound, and Pace define eight, four, and two volumes of points in (a), respectively.

bifurcations occur depend strongly on $\mathbf{W}$ for each attractor. These bifurcations naturally involve collisions with the system's many unstable fixed points that have intricate trajectories in phase space. Despite this complexity, we now show that an upper bound on α^* can be found for a few special, but informative, cases that link the robustness of attractors back to the interaction function H (Fig. 2). To do so, we leverage the system's 1D invariant manifolds using ideas from equivariant bifurcation theory [48]. In the following three examples, we will follow the same template: an attractor will be chosen and then a spatial pattern of heterogeneity $\mathbf{W}$ will be chosen that aligns with a 1D invariant manifold that intersects with that attractor. Direct substitution in Eqs. (4) will then yield a 1D dynamical system parametrized by the heterogeneity strength α. This procedure identifies an upper bound because while the 1D picture identifies bifurcations, stability may change prior due to interactions with fixed points that do not reside on that manifold (and therefore go untracked during the analysis).

We first consider Pace, $\boldsymbol{\theta} = (\pi, 0, \pi)$. The inset of Fig. 8(c) shows the path traced out by Pace in phase space due to two spatial distributions of intrinsic frequency. The first, $\mathbf{W} = (1, 0, -1)$, is parallel to $(D_1^s, D_1^s)_A$ and corresponds to cluster-preserving perturbations (see Table II). The second, $\mathbf{W} = (0, 1, 0)$, is directed along $(D_1^s, 1)_B$ and disrupts the synchrony of Pace's clusters. We analyze the cluster-preserving case by substituting in $\boldsymbol{\theta} = (\eta, 0, -\eta)$ into Eqs. (4), where η is the phase difference *between* clusters. The reduced dynamics are then $\dot{\eta} = \alpha + k[H(-\eta) - H(\eta)] \equiv \alpha + k\psi(\eta)$. Along this manifold, the crossing at $\eta = \pi$ is Pace. Plotting $\dot{\eta}$ in Fig. 9(b) readily shows how shifting the dynamics with α will result in bifurcations that eliminate the antiphase fixed point at $\alpha^* = \pm\psi_{\max}k$, or in dimensionless terms, $\bar{\alpha}^* \sim \pm 1$.

For the second perturbation direction, we consider dynamics along $(D_1^s, D_1^s)_A$ for which the intercluster phase difference is π but the intracluster phase difference is free to change, $\boldsymbol{\theta} = (\pi, \eta, -\pi)$. The dynamics reduce identically, but the interpretation of η is different. Now, $\eta = 0$ is Pace and local minima and maxima on either side determine α^*. Since these local
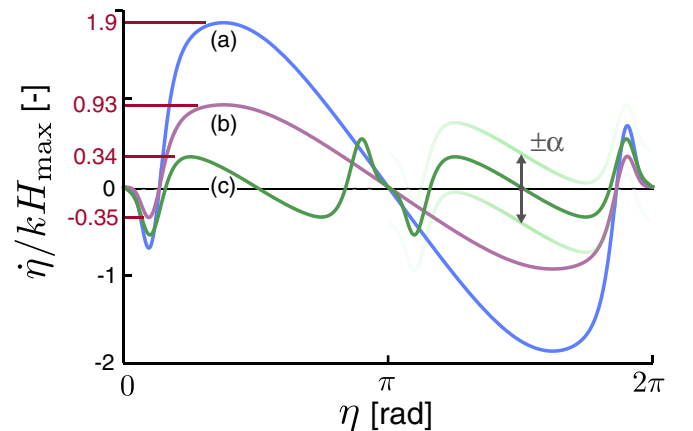

FIG. 9. Dynamics $\dot{\eta} = \alpha + \psi(\eta; k)$ along a selection of invariant manifolds scaled by coupling strength k and $H_{\max}$: (a) intersection of planar IMs $(D_1^p, D_1^p)_A$ and $(D_1^p, D_1^p)_B$, $\boldsymbol{\theta} = (-\eta, \eta, -\eta)$, (b) $(D_1^s, D_1^s)_A$, $\boldsymbol{\theta} = (\eta, 0, -\eta)$ and $(D_1^s, 1)_B$, $\boldsymbol{\theta} = (\pi, \eta, -\pi)$, and (c) $(Z_2, 1)$, $\boldsymbol{\theta} = (\eta, \pi - \eta, \eta)$. Each is used to analyze a different attractor subject to heterogeneity α: (a) Trot ($\eta = \pi$), (b) Pace ($\eta = \pi$ for cluster-preserving perturbations, $\eta = 0$ for cluster breaking), and (c) Gallop ($\eta = \pm\pi/2$). The labeled extrema (red) correspond to the heterogeneity $|\bar{\alpha}|$ at which the fixed points of interest are annihilated through bifurcations.

maxima $< \psi_{\max}$, we conclude that Pace is less structurally robust to cluster-breaking heterogeneity, which is corroborated by the full numerical continuation analysis (Table III).

We can readily extend this approach to the other attractors. For Trot, resilience to cluster-preserving perturbations $\mathbf{W} = (1, -1, 1)$ is found by examining dynamics along $\boldsymbol{\theta} = (\eta, -\eta, \eta)$, which is the intersection of the two planar IMs $(D_1^p, D_1^p)_A$ and $(D_1^p, D_1^p)_B$, where η is the phase difference between the two diagonal clusters. Qualitatively, the dynamics are identical to those considered for Pace, $\dot{\eta} = \alpha + 2k[H(-\eta) - H(\eta)]$. However, a factor of 2 strengthens the effective coupling strength for Trot. It therefore requires twice the heterogeneity to be eliminated, $\bar{\alpha}^* \sim \pm 2$ (Fig. 9). Trot is the strongest in this direction; Table III shows that it is more susceptible to perturbations with clustered rows or columns.

Finally, we consider Gallop, which is only intersected by one invariant manifold, $(Z_2, 1)$. Letting $\boldsymbol{\theta} = (\eta, \pi - \eta, \eta)$ and $\mathbf{W} = (1, -1, 1)$, the dynamics simplify to $\dot{\eta} = \alpha + k[H(-\pi - \eta) + H(-\eta) - H(\eta) - H(\pi - \eta)]$. These dynamics are compared to the reduced dynamics of Pace and Trot in Fig. 9, where the fixed points at $\eta = \pm \pi/2$ are the two Gallop states. They vanish when $\bar{\alpha}$ exceeds the local maxima or minima near them, $\sim \pm 0.34$, which is less than that which annihilates the in-phase and antiphase fixed points for Trot and Pace.

Numerical continuation shows that Gallop's stability changes before annihilation at $\bar{\alpha}^* \sim \pm 0.18$ (Table III). Thus, the invariant manifold analysis gives only an upper bound. Still, the semianalytical examination facilitates intuition about how different interaction functions H might impact stability and robustness to heterogeneity. For example, if $H \sim \sin()$, then dynamics along $(Z_2, 1)$ simplify even further to $\dot{\eta} = \alpha$, which is a marked qualitative difference between the BZ-in-PDMS system and an idealized Kuramoto network.

Between the full numerical continuation and IM analyses, we arrive at an approximate ranking for the relative robustness of the attractors that agrees with experimental observations (in order of most resilient against heterogeneity to least): Trot, Pace/Bound, Pronk, and Gallop. As seen within Fig. 7(c) the theory predicts Trot was stable for nearly all experiments. In contrast, Gallop was rarely stable.

IV. DISCUSSION

We theoretically and experimentally studied a four-ring network of self-driven oscillators. We utilized the H/K theorem to enumerate steady states and other invariant manifolds (IMs) required by symmetry. We developed a phase model faithful to the experimental BZ-in-PDMS system that included chemical details and treated the heterogeneity of the oscillators which allowed us to predict the stability of the steady states and manifolds, and to describe the dynamics. Each invariant manifold predicted by the H/K theorem breaks some symmetry of the underlying network; a notable feature of our experimental system is that the combination of inhibitory and excitatory interactions renders many of these structures stable and therefore experimentally accessible. Inhibitory interactions generated by the high permeability of PDMS to bromine are responsible for the symmetry breaking that stabilizes the Trot state in which every oscillator is out of phase with its nearest neighbor, and excitatory interactions are responsible for stabilizing synchronized nearest neighbors in the Pronk and Pace/Bound states, in which either all (Pronk) or half of the oscillators (Pace/Bound) are in phase. In a purely excitatory-coupled system, all invariant manifolds would still exist, but a fully synchronized (in-phase) state would be the only stable state and therefore would dominate observations. The influence of the other invariant manifolds would be limited to transient behavior. The BZ-in-PDMS network possesses both excitatory and inhibitory coupling, which allowed us to experimentally quantify the coexistence of multiple competing attractors in the network. We note that the complexity of the BZ-in-PDMS interaction function is minimal in the sense that, when placed in the four-ring topology, it renders all H/K fixed points as attractors while producing no additional ones. This feature is serendipitous but underscores the potential benefits of exploring real oscillators rather than idealized ones. By contrast, the Kuramoto model considered in the Supplemental Material [33] (Fig. S7) lacks the rich multistability even though all of the H/K-predicted fixed points are necessarily identical to those in the BZ network.

On the one hand, while previous studies on biological networks have demonstrated some correspondence between observed spatiotemporal patterns and topology, it is difficult to contextualize the observations because the living networks lack a quantitative model of the oscillators and their coupling, and the experiments lacked steady-state conditions [5,49]. On the other hand, electromechanical [7], electrical [6,50], or electrochemical [51] based oscillator networks leverage components engineered to high precision with which the oscillator dynamics and coupling details are known, facilitating transparency between topology and dynamics. However, these systems follow different engineering principles than do biological and synthetic chemical systems and therefore do not shed light on the challenges of building autonomous materials. Hybrid systems that mediate coupling between chemical oscillators through a computer provide a unique degree of control over network dynamics [52,53], including some studying similar networks, including the four-ring network studied here [54–58], but using a computer to control interactions between chemical oscillators means these systems are neither autonomous nor self-organizing. Here, we build on the foundation of the BZ chemical oscillator, which is perhaps the best characterized chemical oscillator in isolation [21,34], to predict network-level phenomena. Our work simultaneously builds an autonomous, self-organizing reaction-diffusion system with multiple attractors and addresses the role of heterogeneity on those spatiotemporal patterns. We measure the dimensionless heterogeneity (Fig. 7), which is the key parameter for controlling the existence of phase-locked states. Through its union of theory and experiment, our work provides an essential linkage between the biological and the engineered.

Kuramoto's work on heterogeneous, weakly coupled pairs provides the essential framework for understanding how frequency differences between oscillators lead to desynchronization [18]. In larger networks this intuition is obfuscated by the higher dimensionality of the system. We show that this complexity can be reduced to that of the pairwise problem

by judiciously choosing particular spatial patterns of heterogeneity that preserve invariant manifolds of the system, and then examining dynamics and bifurcations along them. This analysis confirmed the experimental and computational observations that each attractor had a different response to heterogeneity and that this response depended on the spatial pattern of frequency heterogeneity. Systematically examining heterogeneity for each invariant manifold allows us to use symmetry-derived features of the dynamics to understand the impact of symmetry-breaking heterogeneity. More broadly, our work demonstrates a general methodology, applicable to many networks and oscillator systems, for analyzing the impact of heterogeneity in nature and tailoring its use in engineered systems.

Prior work using group theoretic approaches [8,9] and equitable partitions [59,60] has been particularly fruitful in systematizing the identification of topology-required clustered states. Once symmetries are identified, a master stability function approach is used to determine transverse stability of identified clustered, limit cycle solutions [61]. In contrast, we use the H/K theorem to identify not just clusters, but spatiotemporal patterns described by phase relationships between oscillators. In principle, systematizing application of the H/K theorem to the large, arbitrary networks considered by Pecora *et al.* [8] is possible, but to our knowledge has not been achieved. Another difference with prior work is that we create a phase model of the dynamics in the weak coupling limit, further reduce the dynamics by examining only the relative dynamics between oscillators, and then assess the stability of the fixed points and higher-order invariant manifolds that emerge. However, we note that both the prior work and ours are quantifying the same quality of the network, the ability to phase-lock parts of a network. In our case, as we limit the theory to weak coupling, phenomena associated with higher coupling strength are lost, but we gain the ability to semianalytically analyze bifurcations along 1D manifolds, providing intuition that may be hard to extract via other methods. We note that corrections to the phase model can be systematically introduced [42], but at the cost of adding additional degrees of freedom.

Heterogeneity can impact dynamics in unexpected ways. A recent experimental work on an electromechanical system [62,63] has demonstrated that heterogeneity leads to robustness in the face of system noise through converse symmetry breaking [64]. This work explored the phenomena of symmetry arising from system asymmetry in inertial oscillators; however, it is not known whether there is an analog in the case studied here of weakly coupled networks for which the dynamics are overdamped. Other examples of coupled oscillators also note qualitatively different synchronization phenomena in the face of heterogeneity between strongly and weakly coupled oscillators [53]. Our measurements confirm that we are in a weakly coupled regime and thus our analysis is valid.

Finally, we note limitations of the current study. First, complete experimental control of initial conditions was not achieved. The use of a photosensitive catalyst coupled to a computer controlled light projector was excellent at setting in-phase or antiphase synchrony in experiment. For reasons we have yet to understand, setting other initial conditions,

e.g., Gallop, with the same method often failed. As a result, we could not unambiguously determine if Gallop was fully unstable or possessed an extremely small basin of attraction. Second, experimentally validating the response of fixed points to controlled addition of structured heterogeneity is a natural extension of our work. Control of both initial conditions and heterogeneity would allow an efficient search for the steady states created by heterogeneity, labeled "Other," in Fig. 8(a). Experimentally implementing both is planned as a continuation to this work. Last, we note that the finite lifetime of an experiment, ∼70 oscillations, is insufficient to observe steady states with long convergence times. While sufficient to observe states which are robust to heterogeneity—Pronk, Bound/Pace, and Trot—it may hinder observation of sensitive states that are on the verge of annihilation through a bifurcation. Use of microfluidic reactors that are fed new reactants to create truly open chemical systems, currently yet to be developed, would allow much longer experiments to explore these dynamics.

V. CONCLUSION

Understanding how network structure controls spatiotemporal pattern formation remains a central problem in network science. Analysis of spatial network symmetries has led to great progress by illuminating mechanisms behind the emergence of clustered, dynamical states. Specifically, tools based on group theory [8,9] and equitable partitions [59,60] have been particularly fruitful in systematizing the identification of topology-required clustered states. Theoretically generalizing these methods to predict behaviors in real systems, with mathematically imperfect network structure, is a largely untouched topic, but one essential for elucidating the engineering principles necessary to exploit network symmetries in applications involving chemical networks.

This work represents the most thorough experimental study of a reaction-diffusion network to date with an order of magnitude increase in the longevity of each experiment and the number of experiments performed. Within this work we find consistencies and discrepancies between theoretical predictions and experimental observations of a small reaction-diffusion network of oscillators assuming perfect square symmetry. The majority of attractors are distributed about the values predicted by assuming that the network's nodes and connections are homogeneous. The distributions possess widely varying shapes and one attractor predicted by the idealized theory was altogether absent. We account for these discrepancies between the theory of homogeneous oscillators and experiment by incorporating heterogeneity in the intrinsic frequency of the oscillators using simulations, numerical continuation, and a quasianalytical bifurcation analysis of a phase model in a fashion inspired by Kuramoto. Our multifaceted approach infers there is a small degree of chemical heterogeneity in the system, producing only 3% variations in intrinsic frequencies [21], but which was sufficient to cause major changes to some attractors predicted by symmetry while only weakly altering others. The analytic method we apply is generalizable to any system modeled by a phase model and any topology, requiring only that a number of

1D invariant manifolds be identified. Further, we demonstrate that with proper accounting of heterogeneity, symmetry can be used to rationally engineer spontaneously organizing reaction-diffusion networks, an important category that includes biological systems such as neural networks. In particular, we studied a ring of four chemical oscillators, which symmetry-based theories predict are capable of generating the spatiotemporal patterns known as the gaits of a quadruped. In this work, we experimentally validate that symmetry dictates function in weakly coupled reaction-diffusion systems even in the presence of heterogeneity.

APPENDIX A: EXPERIMENTAL METHODS

1. Network fabrication

The microfluidic reaction-diffusion network was made out of four adjacent reactors embedded in polydimethylsiloxane (PDMS). The reactors are formed out of divots in PDMS that we fill, and then seal with a single piece of glass, forming a common lid for the array. We manufactured these divots using a soft lithographic process in which PDMS is cured while pressed against an inverse (positive) of the divots made out of a photoresist deposited onto a silicon wafer. This was performed as previously published [20], with the exception of one adaptation described below. This generates a glass microscope slide coated with many reactors organized into networks of four reactors, shown in Figs. 1(b) and 1(c) and in Figs. S1 and S2(a) of the Supplemental Material [33].

The dimensions chosen for the network allow for robust coupling between the four nodes in ring topology. By adjusting the sizes and distances between reactors we found that rectangular reactor dimensions 62 μm × 62 μm × 30 μm ($L \times W \times H$) with side-to-side distance 26 μm resulted in strong coupling. The network reactors are organized in a 2×2 grid [Figs. 1(b) and 2(c)] in such a way that nearest-neighbor reactors possess much more shared surface area relative to next-nearest neighbors across the diagonal. This results in a ringlike connectivity, where coupling between nearest neighbors is stronger than across the diagonal. The rectangle of BZ surrounding the network [Fig. 1(c)] is forced into a steady state, setting the concentration of chemicals surrounding the network. During each experiment we observe 9 or 16 coupled, individual networks, separated from one

another by controlled barriers (see Figs. S1(b) and S1(c) of the Supplemental Material [33]).

The only alteration of the procedure in fabricating the PDMS networks published [20] was to change the way in which the PDMS was pressed and cured: instead of a 15-kg lead brick applied for 12 h followed by baking in a 70 °C oven, we used a thermal press applying 90–113 kg set at 70 °C for 2.5 h. This reproducibly kept the PDMS flash at the bottom of the wells to less than 2 μm and reduced the likelihood of wafer fracture (see Fig. S1(d) of the Supplemental Material [33]).

2. Sample holders

In a previous work, BZ laden PDMS reactors were sealed using an acrylic plastic clamp [20]. All experiments were conducted at room temperature. In this work, since the oscillation period of BZ depends on temperature [65], we created a clamp that controlled sample temperatures to within 0.1 °C of 22.0 °C to maximize reproducibility. The clamp's temperature is controlled through a thermistor that measures the temperature of the clamp near the sample and two Peltier (TEC) devices that are managed through a Proportional-Integral-Derivative (PID) feedback loop run on an Arduino (see Fig. S2 of the Supplemental Material [33]). The sample is robustly driven to the clamp's temperature because the clamp possesses a large thermal mass relative to the sample and large thermal contact area with the sample (see Fig. S2 of the Supplemental Material [33]).

Samples are loaded in a manner identical to the previous study [20]. Further details are presented in Appendix A 5 (Protocol).

3. BZ chemical preparation

The BZ loaded into the microfluidic network is first mixed outside the microfluidic device. A 0.36-mL volume of photosensitive BZ is prepared by sequentially adding equal 60-μL volumes of sulfuric acid, sodium bromide, malonic acid, sodium bromate, ferroin, then Tris(2,2'-bipyridyl)dichlororuthenium(II) hexahydrate to an Eppendorf tube, then mixing it with a Vortex mixer. Note that during the sequential pipetting of the chemicals, upon adding the sodium bromate, the solution converts from colorless to a vivid, transparent yellow for 15 s before returning to a colorless state. The output volumes of the pipette used had a measured percent coefficient of variance of 1.2%. The concentrations of the reagents in the final 0.36-mL mixture, and ultimately in the individual BZ microreactors, are in Table IV.

4. Optics

We measured the chemical state of the reactors by measuring their absorbance of green light. Ferroin's absorbance changes drastically between its oxidized and reduced state. The green light is filtered to 515 ± 10 nm, to avoid exciting the photocatalyst, Ru(bipy)$_3$ (see Figs. S3(a) and S3(c) of the Supplemental Material [33]).

Patterns of blue light perturbations were used to set boundary conditions and initial conditions by selectively exciting the photocatalyst (see Figs. S3(a) and S3(b) of the Supplemental

TABLE IV. Final experimental chemical conditions in reactors.

Chemical	Molecular formula	Concentration (mM)
Sulfuric acid	H_2SO_4	80
Sodium bromide	$NaBr$	25
Malonic acid	$C_3H_4O_4$	400
Sodium bromate	$NaBrO_3$	288
Ferroin	$C_{36}H_{24}FeN_6O_4S$	3
Tris(2,2′-bipyridyl) dichlororuthenium(II) hexahydrate	$C_{30}H_{24}Cl_2N_6Ru.6H_2O$	1.2

Material [33]). Boundary conditions were applied by shining light on the rectangle surrounding each network at an intensity that completely inhibited oscillations (see Fig. S3(b) of the Supplemental Material [33]). Initial conditions were set by applying light to the reactors by inhibiting all reactors with light for 300–600 s. Then, the light was turned off at different times from each of the reactors, thus causing them to resume oscillating at different times. The success rate of hitting target initial conditions far from Trot or Pronk was low.

As in previous works [20,27,28], the patterned blue light was periodically turned off and on (period 2 s, 50% duty cycle) to allow image acquisition without the interference of the applied illumination. During some of the experiments, the blue light was homogenized by measuring the heterogeneity with a CCD and iteratively adjusting the applied illumination through a feedback scheme [21].

The light intensity of sample illumination was measured by placing a power meter in the sample plane. The results are similar to previous work [27]: intensity of blue light applied to boundaries, 0.3 ± 0.04 mW cm^{-2}; intensity of blue light applied to reactors during initial condition setting, 1 ± 0.2 mW cm^{-2}; intensity of blue applied light when projector blank or black, 0.09 ± 0.009 mW cm^{-2}; and intensity of 515-nm green sample illumination, ~ 0.1 mW cm^{-2}. Errors, in standard deviations, express variance in average illumination across the whole sample field of view across all experiments, not the variance across the field of view in individual experiments.

5. Protocol

The protocol for an experiment is as follows:

(1) PDMS chip, reentrant window, and O-ring (see Fig. S2(a) of the Supplemental Material [33]) are cleaned with isopropyl alcohol, deionized water, and dried with compressed air. They are left under petri dishes to prevent dust accumulation.

(2) A small batch of BZ solution is prepared as detailed earlier in Appendix A. Solution is left in a dark chamber.

(3) The PDMS chip is plasma (Harrick Plasma - PDC32G) for 3 min at 400 mbars in ambient atmosphere.

(4) The BZ solution is then pipetted into the networks of interest in the PDMS chip as shown in depth in Supplementary Movie S7 of Ref. [20].

(5) Now, with the reentrant window placed approximately above a feature of networks covered by BZ, the reentrant window must be secured firmly and precisely. While viewing the sample using a stereomicroscope with green filtered transmission illumination, the thumbscrews (see Fig. S2 of the

Supplemental Material [33]) are slowly turned, clamping the device. We alternated tightening them in a zigzag pattern, with each tightening of a screw being roughly a 1/8 or less rotation. During this process any bubbles which are present in the reactors should decrease in size until they are invisible. Once all reactors are surrounded by dark outlines (see Fig. S1(a) of the Supplemental Material [33]), there are no shearing distortions to the network, and there are no bubbles, this process is halted.

(6) The clamp and the network with BZ sealed into it are then left in a dark, room temperature chamber until it has been 40 min since the BZ was initially mixed in step 2, typically 20 min.

(7) The clamp is then loaded into the projection illumination microscope (see Fig. S3(c) of the Supplemental Material [33]). Then, a MATLAB code with GUI is used to align a projected pattern onto the sample (see Fig. S3(b) of the Supplemental Material [33]) and initiate temperature control.

(8) Light is projected onto boundaries and sets initial conditions of networks as described earlier in Appendix A. Data are gathered for between 3000 and 24 000 s, ~ 10 and 81 periods of oscillation of each reactor.

(9) In a few experiments a second attempt at setting initial conditions was made.

APPENDIX B: EXPERIMENTAL PHASE-LOCKED CRITERIA

To identify phase-locked states in experiments we require that $\frac{d}{dt}(\phi_i - \phi_j)$ is almost zero and that $\frac{d^2}{dt^2}(\phi_i - \phi_j)$ is also small. We use the following algorithm to identify phase-locked experiments:

(1) Identify the time evolution of the three phase differences $(\theta_{21}, \theta_{32}, \theta_{43})$.

(2) Low-pass them to form $(\overline{\theta_{21}}, \overline{\theta_{32}}, \overline{\theta_{43}})$.

(3) Find the longest region in the time series where the absolute values of each velocity and the average acceleration for the system are below thresholds $\varepsilon_{a,v}$ such that

$$\left| \frac{d}{dt}\overline{\theta_{21}} \right|, \left| \frac{d}{dt}\overline{\theta_{32}} \right|, \left| \frac{d}{dt}\overline{\theta_{43}} \right| < \varepsilon_v$$

and

$$\frac{d}{dt}\frac{1}{3}\left(\left| \frac{d}{dt}\overline{\theta_{21}} \right| + \left| \frac{d}{dt}\overline{\theta_{32}} \right| + \left| \frac{d}{dt}\overline{\theta_{43}} \right| \right) < \varepsilon_a.$$

We use $\varepsilon_v = 2.5 \times 10^4$ rad s^{-1} and $\varepsilon_a = 9 \times 10^{-8}$ rad s^{-2}.

(4) If the longest region is five or more periods (1500 s), we consider the experiment to be phase locked.

TABLE V. Simulation parameters known.

	Description	Value	Unit
	Reagent concentrations		
a	Bromate	288	mM
m	Malonic acid	400	mM
c_o	Total metal ion catalyst	4.2	mM
h	Protons	160	mM
b	Bromomalonic acid	0.12m	mM
	Reaction rates and relevant constants		
k_1		$2 \times 10^6 h$	$M^{-1}\,s^{-1}$
k_2		$2h^2 a$	s^{-1}
k_3		3×10^3	$M^{-1}\,s^{-1}$
k_4		$42ha$	s^{-1}
k_5		$5 \times 10^9 h$	$M^{-1}\,s^{-1}$
k_6		10	s^{-1}
k_7		$29m$	s^{-1}
k_8		$9.3m$	s^{-1}
k_9		b	s^{-1}
k_{10}		$0.05m$	s^{-1}
k_r		2×10^8	$M^{-1}\,s^{-1}$
k_{red}		5×10^6	$M^{-1}\,s^{-1}$
k_I		0	s^{-1}
b_C		0.05	M
c_{min}		$\sqrt{2k_r(k_9 + k_{10})c_o/k_{red}^2}$	M

APPENDIX C: BEST FIT MODEL

1. Fitting to experiments

We fit the model in Eqs. (4) to each experimental time series of phase differences [Fig. 7(b)] by varying the coupling strength k, excitatory coupling ratio k_e, and the set of three intrinsic frequency differences $\boldsymbol{\Delta\omega} = (\Delta\omega_{21}, \Delta\omega_{32}, \Delta\omega_{43})$ to minimize the squared error between theory and experiment. The first experimental data point was used as the initial condition.

Only a selection of the experimental data was used in the fit. First, we excluded early time points for which oscillators had not achieved a similar frequency. This threshold is defined in Appendix A. The final point in an experimental trajectory used in a fitting was halfway between when the phase-locked condition was met and when it was lost or the end of the experiment if it did not unlock. Further details on the transient dynamics are shown in Fig. S4 of the Supplemental Material [33].

The identified best-fit parameters were $\Delta\omega_{ij} \neq 0$, $k = 2 \times 10^{-2}$ s^{-1}, and $k_e = 0.05$. The intrinsic frequency differences divided by coupling rate $\Delta\omega_{ij}/k$ obeyed a Laplacian distribution $\frac{1}{2b}\exp(-\frac{|\Delta\omega_{ij}/k - \mu|}{b})$ with mean $\mu = 0$ and rate parameter $b = 2\pi \times 4 \times 10^{-3}$ rad s^{-1} [Fig. 7(b)]. Dividing these by the maximum of the H function used in the fitting determines a distribution of dimensionless heterogeneity. Further, the fitting required some excitatory coupling $k_e = 0.05$. Table VI summarizes the best-fit values used in subsequent simulations. We also explored the possibility of diagonal coupling when fitting, but found its contribution to the quality of fit to be two orders of magnitude less sensitive compared to nearest-neighbor coupling and frequency heterogeneity.

TABLE VI. Simulation parameters fitted: In "Fit values" and a single number represents the number fit and then used in simulations and theory. If in a fit or simulation values were randomly distributed, the form of the distribution is described by "L(μ, b)" and represents a Laplacian probability density function with mean μ and rate parameter b.

Parameter	Fit values	Unit
	Coupling	
k	2×10^{-2}	s^{-1}
k_e	0.05	1
	Chemical heterogeneity	
$\Delta\omega_{ij}$	L$(0, 2\pi \times 8 \times 10^{-5})$	rad s^{-1}
$\Delta\omega_{ij}/k$	L$(0, 2\pi \times 4 \times 10^{-3})$	rad
$\Delta\omega_{ij}/kH_{max}$	L$(0, 0.2)$	1

The observed distribution in angular frequency differences is commensurate with previous observations in Ref. [21] where we noted a 2% variation in the periods of individual (uncoupled) wells of the same BZ-in-PDMS system. We can compare the present measurements with the previous through the relation $\tau + \Delta\tau = 2\pi/(\omega + \Delta\omega)$. Solving for $\Delta\tau$, letting $\Delta\omega = \sqrt{2}b$ (where $b = 2\pi \times 8 \times 10^{-5}$ from Table VI), and $\tau = 300$ s gives $\Delta\tau \sim 10$ s, or approximately 3% of the total period. Thus, the present variation we infer from fitting the phase model to observed dynamics agrees with the spread in oscillation periods previously measured.

In Sec. SIII of the Supplemental Material [33] we estimate the coupling strength from first principles k_{ideal} and find that the best-fit value is two orders of magnitude less than this calculation [33]. In past works with emulsion droplets the best-fit value of k has been closer to one order of magnitude lower than expected [24,25,28]. Compared to these past experiments on emulsion droplets, the experiments performed here had a much larger amount of oil phase in the form of PDMS surrounding each four-ring network (see Fig. S1 of the Supplemental Material [33]). As Br$_2$ is known to partition into and react with oil and PDMS [32], more PDMS would cause a reduction in inter-reactor coupling. We hypothesize that this is the cause of the discrepancy.

2. Simulations

Simulations without heterogeneity. The dynamics, Eqs. (4), were implemented using the CHEBFUN Toolbox [66] and integrated using MATLAB's ODE45 with relative and absolute tolerances of 1×10^{-10}.

A dense, uniform sampling of half of the state space, 62 251 simulations in total, was used to determine the size of each attractor's basin of attraction [Fig. 5(b)]. An additional set of 5399 simulations was run that densely sampled initial conditions in the θ_{21} and θ_{43}, but coarsely in θ_{32}, to generate the slices shown in Fig. 5(a).

Simulations with heterogeneity. In running simulations from a dense set of initial conditions, each initial condition had seven simulations initialized from it with independent resamplings of frequency heterogeneity. We thus could observe the impact of heterogeneity throughout state space by sampling the distribution of heterogeneity in all regions of

state space. The results of 34 713 such simulations are shown in Fig. 8(b).

To determine the impact of experimentally realistic heterogeneity on the model, we ran simulations of Eq. (3) with the experimental best-fit parameters in Table VI. Specifically, we included heterogeneity in intrinsic frequencies in our simulations, with $\Delta\omega_{ij}$ drawn from the measured Laplacian distribution defined in Table VI, with mean zero and rate parameter $2\pi \times 8 \times 10^{-5}$ rad s^{-1}, while all other parameters are the constant value enumerated in the third row.

3. Phase model reduction

In the limit of weak coupling, the dynamics of each oscillator in a network can be reduced through the introduction of a coupling function H. This nonlinear function quantifies how mass transport dynamically alters the phases of connected oscillators. To determine this function for our system, we first identify the phase response curves (PRCs) **Q** of the Vanag-Epstein model using Malkin's adjoint method [40–42,44]. **Q** quantifies the *phase-dependent* response of an oscillator's phase due to infinitesimal chemical perturbations $\delta\mathbf{c}$ such that $\delta\phi = \mathbf{Q}(\phi) \cdot \delta\mathbf{c}$. In our case there are four curves, one for each chemical species in the VE model.

The instantaneous rate of change of an oscillator i's phase due to interactions with the jth oscillator is denoted F_{ij} and is proportional to the dot product of **Q** and the mass flux **g** (M s^{-1}), $F_{ij}(\phi_i, \phi_j) = \mathbf{Q}(\phi_i) \cdot \mathbf{g}(\phi_i, \phi_j)$. Since the mass flux is driven by concentration differences between oscillators, we set $\mathbf{g}(\phi_i, \phi_j) = \mu[\mathbf{c}_{LC}(\phi_j) - \mathbf{c}_{LC}(\phi_i)]$, where the dynamic concentrations are that of an isolated oscillator and the matrix μ is identical to the one in Eq. (1). The ability to use the pretabulated concentration dynamics in generating the interaction function is key to the model reduction process. Importantly, it is an approximation valid in the weak coupling limit; in general, oscillator interactions will perturb the oscillators off of their uncoupled limit cycles.

The complete phase dynamics of each oscillator are then given by the sum of all internode interactions and the intrinsic frequency ω_i such that $\frac{d}{dt}\phi_i = \omega_i + \sum_j A_{ij} F(\phi_i, \phi_j)$. For our system, multiple species diffuse across the PDMS barrier. F is therefore the linear combination of the flux due to Br$_2$, u, and HBrO$_2$, x, such that

$$F(\phi_i, \phi_j) = k[Q_u(\phi_i)(u_{LC}(\phi_j) - u_{LC}(\phi_i))$$
$$+ k_e Q_x(\phi_i)(x_{LC}(\phi_j) - x_{LC}(\phi_i))]. \quad (C1)$$

We can further simplify the dynamics by assuming that the phase difference $\phi_j - \phi_i$ evolves slowly compared to the intrinsic frequency, and period-average the interaction. We introduce the interaction function H such that

$$H_{ij}(\phi_j - \phi_i) \equiv k^{-1}(2\pi)^{-1} \int_0^{2\pi} F(\alpha, \alpha + \phi_j - \phi_i) d\alpha. \quad (C2)$$

Typically, the coupling rate k (s^{-1}) is incorporated into H. Here, we have divided by the coupling strength to make the coupling strength dependence in Eqs. (4) explicit. We express the interaction function H as the sum of two terms arising from the form of Eq. (C1). The final expression is then

$$H(\phi_j - \phi_i) = H_u(\phi_j - \phi_i) + k_e H_x(\phi_j - \phi_i). \quad (C3)$$

APPENDIX D: METRIC OF DISTANCE

To measure distances between two points in the state space of the 3D phase difference dynamics, we found a surprising function $d(\boldsymbol{\theta}, \boldsymbol{\theta}')$ was required. For a given pair of points $\boldsymbol{\theta}$ and $\boldsymbol{\theta}'$ d is calculated by the following algorithm:

(1) Consider two points in the state space: $\boldsymbol{\theta}' = (\theta'_{21}, \theta'_{32}, \theta'_{43})$ and $\boldsymbol{\theta} = (\theta_{21}, \theta_{32}, \theta_{43})$.

(2) Compute the phase difference of the fourth edge, which is completely determined by the other three, $\boldsymbol{\theta}'_f = (\theta'_{21}, \theta'_{32}, \theta'_{43}, \theta'_{21} + \theta'_{32} + \theta'_{43}) = (\theta'_{21}, \theta'_{32}, \theta'_{43}, \theta'_{41})$ and $\boldsymbol{\theta}_f = (\theta_{21}, \theta_{32}, \theta_{43}, \theta_{41})$.

(3) Define a vector of phase difference between states with $\angle$ being complex, or phasor, angle, $\theta_{\text{diff}_j} = \angle \exp(i * (\theta'_{f_j} - \theta_{f_j}))$.

(4) Let the distance between $\boldsymbol{\theta}'$ and $\boldsymbol{\theta}$ be the Euclidean norm of the 4D phase difference vector, $d(\boldsymbol{\theta}, \boldsymbol{\theta}') = |\boldsymbol{\theta}_{\text{diff}}|_2$.

APPENDIX E: COMPUTING TRANSVERSE STABILITY OF INVARIANT MANIFOLDS

1. Point invariant manifolds (fixed points)

Traditional linear stability analysis determines the stability of the point invariant manifolds. A given point invariant manifold $\boldsymbol{\theta}^\dagger$, at which by definition $\boldsymbol{\Psi}(\boldsymbol{\theta}^\dagger) = 0$, is stable when the Jacobian $J = \nabla_{\boldsymbol{\theta}} \boldsymbol{\Psi}|_{\boldsymbol{\theta}^\dagger}$ has eigenvalues with real part which are all strictly negative. This 3×3 matrix is written explicitly in Sec. SIV, Eq. (S2), of the Supplemental Material [33]. The maximum real eigenvalue λ^* of all steady states of the model, including the attractors discussed in the paper, are listed in Figs. S6 and S7 of the Supplemental Material [33].

2. Higher-order invariant manifolds

The maximum transverse eigenvalue λ^* of higher-order invariant manifolds determines whether trajectories will locally collapse to or diverge from them [67]. λ^* can be computed at the phase model level by linearizing the dynamics in Eqs. (4) about the invariant manifolds [8,16,61,67,68]. The analysis is simplified by the fact that all the IMs enumerated by the H/K theorem are linear geometric objects with explicit representations. This simplification is a consequence of choosing to represent the network's dynamics in phase difference space.

We begin by considering whether a trajectory $\boldsymbol{\theta}'(t)$ perturbed off an invariant manifold with displacement $\delta\boldsymbol{\theta}$ will converge back to or diverge from the manifold. For small displacements, the dynamics can be linearized around the trajectory that lies on the manifold by letting $\boldsymbol{\theta} = \boldsymbol{\theta}' + \delta\boldsymbol{\theta}$ and expanding the dynamics $\boldsymbol{\Psi}$ [Eqs. (4)] for small $\delta\boldsymbol{\theta}$:

$$\frac{d}{dt}(\boldsymbol{\theta}' + \delta\boldsymbol{\theta}) = \boldsymbol{\Psi}(\boldsymbol{\theta}' + \delta\boldsymbol{\theta})$$
$$\approx \boldsymbol{\Psi}(\boldsymbol{\theta}') + J\delta\boldsymbol{\theta} + \mathcal{O}(\delta\boldsymbol{\theta}^2), \quad (E1)$$

where $J = \nabla_{\boldsymbol{\theta}} \boldsymbol{\Psi}|_{\boldsymbol{\theta}'}$ is the Jacobian evaluated along a trajectory on an IM. Since we are only interested in whether or not perturbations decay or grow, we consider the leading-order dynamics of the perturbation relative the manifold trajectory $\boldsymbol{\theta}'$:

$$\frac{d}{dt}\delta\boldsymbol{\theta} = J\delta\boldsymbol{\theta}. \quad (E2)$$

We now project the perturbation and its dynamics onto a basis aligned with an invariant manifold using the unitary transformation matrix $P = [\mathbf{t}_1, \ldots, \mathbf{n}_1, \ldots]^T$, where $\mathbf{t}_i$ and $\mathbf{n}_i$ are, respectively, the set of unit vectors tangent to and normal to the manifold that form an orthonormal basis. The unit vectors in P are defined in terms of the original basis, e.g., $\mathbf{t}_i = (\mathbf{t}_i \cdot \mathbf{e}_{\theta_{21}}, \mathbf{t}_i \cdot \mathbf{e}_{\theta_{32}}, \mathbf{t}_i \cdot \mathbf{e}_{\theta_{43}})$. By defining a new perturbation $\boldsymbol{\xi} = P \cdot \delta\boldsymbol{\theta}$ and multiplying both sides of Eq. (E2) by P, we can transform the dynamics of perturbations to the following:

$$\frac{d}{dt}(P \cdot \delta\boldsymbol{\theta}) = PJ\delta\boldsymbol{\theta} \Rightarrow \frac{d}{dt}\boldsymbol{\xi} = PJP^{-1}\boldsymbol{\xi}. \quad \text{(E3)}$$

The properties of the resulting matrix $J' = PJP^{-1}$ determine manifold stability. First, we are only interested in perturbations off of the manifold, $\delta\boldsymbol{\theta} \in [\mathbf{n}_1, \mathbf{n}_2, \ldots]$. Perturbations along the manifold cannot produce dynamics that carry trajectories off it because normal dynamics are always zero by definition everywhere along IMs such that $\boldsymbol{\Psi} \cdot \mathbf{n}_i|_{\theta'} = 0$. Second, tangent dynamics of $\boldsymbol{\xi}$ that might result from normal perturbations also do not contribute to the perturbed trajectories convergence or divergence from the manifold [67]. We can therefore focus on the block of J' that corresponds to normal dynamics in response to normal perturbations. This block will be a $C \times C$ matrix where C is the system dimension minus the dimension of the manifold. In our case, $C = 1$ or 2 for, respectively, planar and linear IMs; examples are shown in the Supplemental Material [33]. The maximum real eigenvalue of this block λ^* then determines the linear stability of the manifold.

3. Algorithm

We summarize the process described above as follows:

(1) Choose an invariant manifold M, of dimension k, in an n-node network.

(2) Determine k orthonormal vectors which span M and label them the tangent vectors T. Determine a set N of $C = n - 1 - k$ vectors orthonormal to one another and T. We use the Gram-Schmidt procedure.

(3) Compute a unitary transformation matrix P, with the first columns composed of invariant manifold tangents, then followed by normals.

(4) Compute the Jacobian $J(\boldsymbol{\theta}')$ of the system dynamics at points on the invariant manifold $\boldsymbol{\theta}'$.

(5) Transform the Jacobian into its tangent and normal components using P, $J'(\boldsymbol{\theta}') = P \cdot J(\boldsymbol{\theta}') \cdot P^{-1}$.

(6) Extract the block of J' that contains the decoupled transverse dynamics—the columns and rows corresponding to normal components.

(7) Compute the maximum real eigenvalue of the normal block $\lambda^*(\boldsymbol{\theta}')$.

An example outcome of this procedure for the (D_1^p, D_1^p) invariant manifold is shown in Sec. SIVA of the Supplemental Material [33]. Generic expressions of the block of J' for all invariant manifolds of a broad class of four-ring networks are computed in terms of first derivatives of H in Table SII of the Supplemental Material [33]. A comparison between the stability of manifolds of a four-ring network of Kuramoto oscillators to our system is presented in Fig. S9 of the Supplemental Material [33].
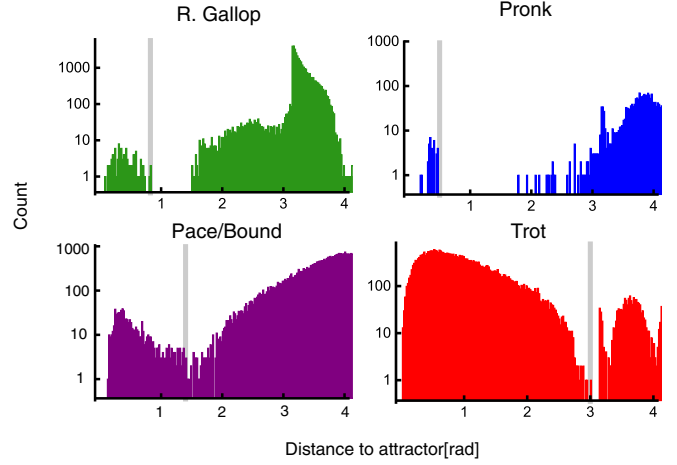

FIG. 10. Histograms of the distances of phase-locked steady states generated by heterogeneous simulations to each H/K attractor. The cutoffs (gray bars) denote the end of the distribution, which are either local minima or the points at which the count drops to zero. These distances are, respectively, 0.825, 0.5, 1.4, and 3.0 rad for Gallop, Pronk, Pace, and Trot.

APPENDIX F: NUMERICAL CONTINUATION TO COMPUTE BIFURCATION DIAGRAMS

(1) MATCONT was used to compute the loss of stability of attractors to heterogeneity [69]. To this end we set up MATCONT to continue the attractors in the $\overline{\Delta\omega} = 0$ case in different directions $\boldsymbol{\Delta\omega} = \alpha\mathbf{W}$, each parametrized by a single parameter α. MATCONT was set to run until discovering loss of stability and not further. During this limited analysis we observed Limit (Saddle-Node) and Branch (Transcritical) points as well as Hopf bifurcations.

(2) We found it was essential to pose the problem carefully otherwise the MATCONT solver was unable to continue the problem. First, it was essential we represent the interaction function H as a Chebyshev function [66]. This alone required us to use the script based CL_MATCONT (version 6.11) instead of the GUI based version. We also needed to provide a symbolic Jacobian of the system, with $\frac{d}{d\chi}H(\chi)$ approximated using derivatives of the Chebyshev represented H. Third, we needed to provide the Jacobian of the dynamics $\boldsymbol{\Psi}$ with respect to the parameters $\mathbf{W}$. We use the options MaxStepSize, 1×10^{-3}; MinStepSize, 1×10^{-8}; FunTolerance, 1×10^{-9}; VarTolerance, 1×10^{-11}; TestTolerance, 1×10^{-11}; Singularities, 1; Eigenvalues, 1; InitStepSize, 1×10^{-11}; MaxCorrIters, 20; MaxNewtonIters, 3; SymDerivative, 2; and SymDerivativeP, 1.

APPENDIX G: STATE CLASSIFICATION METHOD

Experimentally observed steady states are associated with an H/K attractor using heterogeneous phase model simulations as a guide using the following protocol:

(1) Compute the distances between steady states from simulation and all H/K attractors.

(2) Assemble histograms of the distances. Figure 10 shows the histograms for each H/K attractor.

(3) For each histogram, determine a threshold distance d_A at which the first peak decays to zero or is a local minimum.

(4) For an experimentally observed steady state, if it falls within the distance d_A of an attractor, assign it to that attractor.

Otherwise, if the steady state's location is further than the threshold for all attractors, assign it to the Other category.

---

[1] S. H. Strogatz, Exploring complex networks, Nature (London) **410**, 268 (2001).

[2] N. Kopell and G. B. Ermentrout, Coupled oscillators and the design of central pattern generators, Math. Biosci. **90**, 87 (1988).

[3] M. Golubitsky, I. Stewart, P. L. Buono, and J. J. Collins, Symmetry in locomotor central pattern generators and animal gaits, Nature (London) **401**, 693 (1999).

[4] A. E. Motter, S. A. Myers, M. Anghel, and T. Nishikawa, Spontaneous synchrony in power-grid networks, Nat. Phys. **9**, 191 (2013).

[5] A. Takamatsu, R. Tanaka, H. Yamada, T. Nakagaki, T. Fujii, and I. Endo, Spatiotemporal Symmetry in Rings of Coupled Biological Oscillators of *Physarum* Plasmodial Slime Mold, Phys. Rev. Lett. **87**, 078102 (2001).

[6] V. In, A. Kho, J. D. Neff, A. Palacios, P. Longhini, and B. K. Meadows, Experimental Observation of Multifrequency Patterns in Arrays of Coupled Nonlinear Oscillators, Phys. Rev. Lett. **91**, 244101 (2003).

[7] M. H. Matheny, J. Emenheiser, W. Fon, A. Chapman, A. Salova, M. Rohden, J. Li, M. H. de Badyn, M. Pósfai, L. Duenas-Osorio, M. Mesbahi, J. P. Crutchfield, M. C. Cross, R. M. D'Souza, and M. L. Roukes, Exotic states in a simple network of nanoelectromechanical oscillators, Science **363**, eaav7932 (2019).

[8] L. M. Pecora, F. Sorrentino, A. M. Hagerstrom, T. E. Murphy, and R. Roy, Cluster synchronization and isolated desynchronization in complex networks with symmetries, Nat. Commun. **5**, 4079 (2014).

[9] F. Sorrentino, L. M. Pecora, A. M. Hagerstrom, T. E. Murphy, and R. Roy, Complete characterization of the stability of cluster synchronization in complex dynamical networks, Sci. Adv. **2**, e1501737 (2016).

[10] F. Sorrentino and L. Pecora, Approximate cluster synchronization in networks with symmetries and parameter mismatches, Chaos **26**, 094823 (2016).

[11] P. Ashwin and J. W. Swift, The dynamics of *n* weakly coupled identical oscillators, J. Nonlinear Sci. **2**, 69 (1992).

[12] M. Golubitsky and I. Stewart, in *The Symmetry Perspective From Equilibrium to Chaos in Phase Space and Physical Space*, 1st ed. (Birkhauser Verlag, Basel, 2000), pp. 59–79.

[13] M. Golubitsky and I. Stewart, Nonlinear dynamics of networks: The groupoid formalism, Bull. Am. Math. Soc. **43**, 305 (2006).

[14] I. Stewart and M. Golubitsky, Symmetry methods in mathematical biology, São Paulo J. Math. Sci. **9**, 1 (2015).

[15] M. Golubitsky and I. Stewart, Rigid patterns of synchrony for equilibria and periodic cycles in network dynamics, Chaos **26**, 094803 (2016).

[16] G. Russo and J.-J. E. Slotine, Symmetries, stability, and control in nonlinear systems and networks, Phys. Rev. E **84**, 041929 (2011).

[17] A. Turing, The chemical basis of morphogenesis, Philos. Trans. R. Soc. London, Ser. B **237**, 37 (1952).

[18] Y. Kuramoto, in *Chemical Oscillations, Waves, and Turbulence*, 1st ed. (Springer-Verlag, Berlin, 1984), p. 156.

[19] M. Golubitsky and I. Stewart, in *The Symmetry Perspective from Equilibrium to Chaos in Phase Space and Physical Space*, 1st ed. (Birkhauser Verlag, Basel, 2000), pp. 1–337.

[20] T. Litschel, M. M. Norton, V. Tserunyan, and S. Fraden, Engineering reaction-diffusion networks with properties of neural tissue, Lab Chip **18**, 714 (2018).

[21] J. Sheehy, I. Hunter, M. E. Moustaka, S. A. Aghvami, Y. Fahmy, and S. Fraden, Impact of PDMS-based microfluidics on Belousov-Zhabotinsky chemical oscillators, J. Phys. Chem. B **124** (2020).

[22] A. Takamatsu, Spontaneous switching among multiple spatiotemporal patterns in three-oscillator systems constructed with oscillatory cells of true slime mold, Physica D **223**, 180 (2006).

[23] A. M. Tayar, E. Karzbrun, V. Noireaux, and R. H. Bar-Ziv, Synchrony and pattern formation of coupled genetic oscillators on a chip of artificial cells, Proc. Natl. Acad. Sci. USA **114**, 11609 (2017).

[24] N. Li, J. Delgado, H. O. González-Ochoa, I. R. Epstein, and S. Fraden, Combined excitatory and inhibitory coupling in a 1-D array of Belousov-Zhabotinsky droplets, Phys. Chem. Chem. Phys. **16**, 10965 (2014).

[25] M. M. Norton, N. Tompkins, B. Blanc, M. C. Cambria, J. Held, and S. Fraden, Dynamics of Reaction-Diffusion Oscillators in Star and Other Networks with Cyclic Symmetries Exhibiting Multiple Clusters, Phys. Rev. Lett. **123**, 148301 (2019).

[26] M. Toiya, H. O. González-Ochoa, V. K. Vanag, S. Fraden, and I. R. Epstein, Synchronization of chemical micro-oscillators, J. Phys. Chem. Lett. **1**, 1241 (2010).

[27] J. Delgado, N. Li, M. Leda, H. O. González-Ochoa, S. Fraden, and I. R. Epstein, Coupled oscillations in a 1D emulsion of Belousov-Zhabotinsky droplets, Soft Matter **7**, 3155 (2011).

[28] N. Tompkins, N. Li, C. Girabawe, M. Heymann, G. B. Ermentrout, I. R. Epstein, and S. Fraden, Testing Turing's theory of morphogenesis in chemical cells, Proc. Natl. Acad. Sci. USA **111**, 4397 (2014).

[29] N. Tompkins, M. C. Cambria, A. L. Wang, M. Heymann, and S. Fraden, Creation and perturbation of planar networks of chemical oscillators, Chaos **25**, 064611 (2015).

[30] N. Li, N. Tompkins, H. Gonzalez-Ochoa, and S. Fraden, Tunable diffusive lateral inhibition in chemical cells, Eur. Phys. J. E **38**, 1 (2015).

[31] A. L. Wang, J. M. Gold, N. Tompkins, M. Heymann, K. I. Harrington, and S. Fraden, Configurable NOR gate arrays from Belousov-Zhabotinsky micro-droplets, Eur. Phys. J.: Spec. Top. **225**, 211 (2016).

[32] M. E. Moustaka, M. M. Norton, B. Blanc, V. Horvath, S. A. Aghvami, and S. Fraden, Partition, reaction, and diffusion coefficients of bromine in elastomeric polydimethylsiloxane, J. Phys. Chem. B **125**, 5937 (2021).

[33] See Supplemental Material at http://link.aps.org/supplemental/10.1103/PhysRevE.105.024310 for movies and details concerning experimental methods, numerical simulations, and theory.

[34] V. K. Vanag and I. R. Epstein, A model for jumping and bubble waves in the Belousov-Zhabotinsky-aerosol OT system, J. Chem. Phys. **131**, 104512 (2009).

[35] K. Torbensen, F. Rossi, S. Ristori, and A. Abou-Hassan, Chemical communication and dynamics of droplet emulsions in networks of Belousov-Zhabotinsky micro-oscillators produced by microfluidics, Lab Chip **17**, 1179 (2017).

[36] I. S. Proskurkin and V. K. Vanag, Dynamics of a 1D array of inhibitory coupled chemical oscillators in microdroplets with global negative feedback, Phys. Chem. Chem. Phys. **20**, 16126 (2018).

[37] K. Torbensen, S. Ristori, F. Rossi, and A. Abou-Hassan, Tuning the chemical communication of oscillating microdroplets by means of membrane composition, J. Phys. Chem. C **121**, 13256 (2017).

[38] V. K. Vanag and I. R. Epstein, Excitatory and inhibitory coupling in a one-dimensional array of Belousov-Zhabotinsky micro-oscillators: Theory, Phys. Rev. E **84**, 066209 (2011).

[39] A. T. Winfree, Biological rhythms and the behavior of populations of coupled oscillators, J. Theor. Biol. **16**, 15 (1967).

[40] G. B. Ermentrout and D. H Terman, in *Mathematical Foundations of Neuroscience*, 1st ed., edited by S. S. Antman, J. E. Marsden, L. Sirovich, and S. Wiggins (Springer, New York, 2009), Vol. 8, pp. 171–216.

[41] M. A. Schwemmer and T. J. Lewis, The theory of weakly coupled oscillators, in *Phase Response Curves in Neuroscience: Theory, Experiment, and Analysis* (Springer, New York, NY, 2012), pp. 3–30.

[42] D. Wilson and B. Ermentrout, Augmented phase reduction of (not so) weakly perturbed coupled oscillators, SIAM Rev. **61**, 277 (2019).

[43] B. Monga, D. Wilson, T. Matchen, and J. Moehlis, Phase reduction and phase-based optimal control for biological systems: A tutorial, Biol. Cybern. **113**, 11 (2019).

[44] E. Izhikevich, in *Dynamical Systems in Neuroscience* (MIT Press, Cambridge, MA, 2006), pp. 435–478.

[45] M. Giver, Z. Jabeen, and B. Chakraborty, Phase and frequency entrainment in locally coupled phase oscillators with repulsive interactions, Phys. Rev. E **83**, 046206 (2011).

[46] S. Strogatz, *Nonlinear Dynamics and Chaos: With Applications to Physics, Biology, Chemistry, and Engineering*, 1st ed. (Perseus Books, New York, 1994).

[47] We note that it is unexpected to find a Laplacian distribution given the observations of Ref. [21]. One explanation for this is that the underlying distribution of oscillator frequencies is Gaussian, but by focusing our analysis on only those experiments that phase lock, we omit the extremes, reshaping the measured distribution.

[48] P. Chossat and R. Lauterbach, in *Methods in Equivariant Bifurcations and Dynamical Systems*, 1st ed. (World Scientific, River Edge, NJ, 2000), p. 154.

[49] A. Takamatsu, T. Fujii, and I. Endo, Time Delay Effect in a Living Coupled Oscillator System with the Plasmodium of Physarum polycephalum, Phys. Rev. Lett. **85**, 2026 (2000).

[50] S. K. Dana, B. Blasius, and J. Kurths, Experimental evidence of anomalous phase synchronization in two diffusively coupled Chua oscillators, Chaos **16**, 023111 (2006).

[51] C. Bick, M. Sebek, and I. Z. Kiss, Robust Weak Chimeras in Oscillator Networks with Delayed Linear and Quadratic Interactions, Phys. Rev. Lett. **119**, 168301 (2017).

[52] J. F. Totz, R. Snari, D. Yengi, M. R. Tinsley, H. Engel, and K. Showalter, Phase-lag synchronization in networks of coupled chemical oscillators, Phys. Rev. E **92**, 022819 (2015).

[53] D. Wilson, S. Faramarzi, J. Moehlis, M. R. Tinsley, and K. Showalter, Synchronization of heterogeneous oscillator populations in response to weak and strong coupling, Chaos **28**, 123114 (2018).

[54] I. S. Proskurkin, P. S. Smelov, and V. K. Vanag, Experimental investigation of the dynamical modes of four pulse-coupled chemical micro-oscillators, ChemPhysChem **20**, 2162 (2019).

[55] P. S. Smelov, I. S. Proskurkin, and V. K. Vanag, Controllable switching between stable modes in a small network of pulse-coupled chemical oscillators, Phys. Chem. Chem. Phys. **21**, 3033 (2019).

[56] I. S. Proskurkin, P. S. Smelov, and V. K. Vanag, Experimental verification of an opto-chemical "neurocomputer", Phys. Chem. Chem. Phys. **22**, 19359 (2020).

[57] P. S. Smelov and V. K. Vanag, Experimental investigation of a unidirectional network of four chemical oscillators pulse-coupled through an inhibitor, Russ. J. Phys. Chem. A **91**, 1015 (2017).

[58] D. A. Safonov, V. V. Klinshov, and V. K. Vanag, Dynamical regimes of four oscillators with excitatory pulse coupling, Phys. Chem. Chem. Phys. **19**, 12490 (2017).

[59] I. Belykh and M. Hasler, Mesoscale and clusters of synchrony in networks of bursting neurons, Chaos **21**, 016106 (2011).

[60] A. B. Siddique, L. Pecora, J. D. Hart, and F. Sorrentino, Symmetry- and input-cluster synchronization in networks, Phys. Rev. E **97**, 042217 (2018).

[61] L. M. Pecora and T. L. Carroll, Master Stability Functions for Synchronized Coupled Systems, Phys. Rev. Lett. **80**, 2109 (1998).

[62] F. Molnar, T. Nishikawa, and A. E. Motter, Network experiment demonstrates converse symmetry breaking, Nat. Phys. **16**, 351 (2020).

[63] F. Molnar, T. Nishikawa, and A. E. Motter, Asymmetry underlies stability in power grids, Nat. Commun. **12**, 1457 (2021).

[64] T. Nishikawa and A. E. Motter, Symmetric States Requiring System Asymmetry, Phys. Rev. Lett. **117**, 114101 (2016).

[65] T. Bánsági, M. Leda, M. Toiya, A. M. Zhabotinsky, and I. R. Epstein, High-frequency oscillations in the Belousov-Zhabotinsky reaction, J. Phys. Chem. A **113**, 5644 (2009).

[66] T. A. Driscoll, N. Hale, and L. N. Trefethen, *Chebfun Guide*, 5th ed. (Pafnuty Publications, Oxford, 2014).

[67] P. Ashwin, J. Buescu, and I. Stewart, From attractor to chaotic saddle: A tale of transverse instability, Nonlinearity **9**, 703 (1996).

[68] V. N. Belykh, I. V. Belykh, and K. V. Nelvidin, Spatiotemporal synchronization in lattices of locally coupled chaotic oscillators, Math. Comput. Simul. **58**, 477 (2002).

[69] A. Dhooge, W. Govaerts, and Y. A. Kuznetsov, MATCONT: A MATLAB package for numerical bifurcation analysis of ODEs, ACM Trans. Math. Software **29**, 141 (2003).